Leveraging Quasi-Periodic Orbits to Design Transfers in the Circular Restricted Three-Body Problem

Dhruv Jain* and Kathleen C. Howell†
Purdue University, West Lafayette, IN, 47907, USA

For a viable cislunar space infrastructure, the transfer trajectories between various types of host orbits require reasonable maneuver costs and flight times. Multiple transfer design frameworks are presented that leverage the hyperbolic invariant manifolds associated with quasi-periodic orbits to uncover transfers between periodic orbits with different stability properties. The two problems addressed by the described framework are (i) transfers between nearly/marginally stable periodic orbits that lack useful hyperbolic manifolds and (ii) transfers between unstable periodic orbits in the same orbit family. Quasi-periodic orbits, when applied to the design of transfers between an L_2 9:2 NRHO and a DRO (both stable orbits), yield two types of transfers: two-maneuver interior-type and three-maneuver exterior-type transfers. The selected QPOs leveraged to design the transfer pathways assist in realizing a greater number of transfer options that are of lower maneuver cost than the solutions derived from their underlying periodic orbits. For the unstable periodic orbits, two strategies are utilized to design transfers. Firstly, locally fuel-optimal transfers are computed between L_1 halo orbits and they unveil a linear correlation between the total maneuver cost and the difference in out-of-plane amplitude of the departure and arrival orbits. Secondly, another strategy utilizes the unstable manifolds associated with QPOs to design *1-parameter* families of solutions. The geometry and maneuver cost of the QPO-derived solutions are comparable to the locally fuel-optimal transfers. Additionally, the QPO-informed transfers assist in realizing connections between a larger range of departure and arrival locations.

I. Introduction

There is a renewed interest in returning to the Moon and establishing a sustainable space economy in the cislunar region from a number of governmental agencies and private companies [1–5]. Currently, the main focus for NASA's strategy is a space station, i.e., Gateway, in an L_2 9:2 synodic resonant Near-Rectilinear Halo Orbit (NRHO) to enable frequent transfers between Orion, lunar landers, and other future cislunar space assets [6]. In addition, in the recent Artemis 1 mission, the Orion vehicle leveraged a Distant Retrograde Orbit (DRO) to remain in the vicinity of the Moon to test the vehicle's capabilities [7]. But there are multiple periodic orbits of interest, and to create a viable cislunar space infrastructure, transfer trajectories between various host orbits require different design frameworks for various sets of applications.

For a viable space economy, the transfer trajectories require reasonable maneuver costs and flight times, as well as operational feasibility. Due to the variety of host orbits and the infinite solution space, it is worthwhile to leverage fundamental dynamical structures. Preliminary trajectory design in the multi-body regime is challenging due to the complex interplay of the Earth and Moon gravity. However, the Circular Restricted Three-Body Problem (CR3BP) simplifies the analysis by relying on foundational dynamical behaviors. The flow in the CR3BP is characterized by equilibrium, periodic, and quasi-periodic solutions, and their associated invariant manifolds [8]. The stable/unstable manifolds for the generally well-behaved solutions in the CR3BP model allow for the design of complex transfer geometries as exemplified by the GENESIS [9] and the 2010 ARTEMIS mission [10]. Various classes of transfers are rooted in the different dynamical structures to deliver initial guesses incorporating mission-specific operational constraints and yield desired geometries in higher-fidelity models.

This investigation proposes multiple trajectory design frameworks that leverage the hyperbolic invariant manifolds associated with *2-dimensional* quasi-periodic orbits (QPOs) to construct transfers between different types of periodic orbits. These frameworks address two distinct problems: (i) transfers between nearly/marginally stable periodic orbits that lack useful hyperbolic manifolds, and (ii) transfers between unstable spatial periodic orbits within the same

*M.S. Student, School of Aeronautics and Astronautics, dhruvj9922@gmail.com
†Hsu Lo Distinguished Professor, School of Aeronautics and Astronautics, howell@purdue.edu, AIAA and AAS Fellow.

orbit family, which possess hyperbolic manifolds. The formulated step-by-step frameworks reduce the complexity of employing the *5-dimensional* manifolds associated with the *2-parameter* family of QPOs to design feasible transfer geometries. Initial guesses for the design problems are identified through an events function that leverages the continuous representations of periodic orbits and Poincaŕe maps. For transfers between nearly/marginally stable periodic orbits, two types of geometries—interior-type and exterior-type—are uncovered through differential correction schemes. These pathways, informed by QPOs, link departure and arrival orbits through two/three impulsive maneuver transfers. Additionally, locally fuel-optimal geometries are realized by employing an optimization scheme. Subsequently, the transfer trajectories that are constructed through QPOs are compared with the ones that are informed by periodic orbits underlying the selected QPOs. The transfers between unstable periodic orbits in the same family are constructed via the unstable manifolds associated with QPOs. The QPO-derived transfers are compared with the locally fuel-optimal transfers that are generated through the initial guess design strategy proposed by Gómez et al. [11]. The presented frameworks provide methodologies that leverage the stable and unstable manifolds associated with QPOs to enhance the known transfer options between different types of periodic orbits.

II. Background

A. Dynamical Model

The Circular Restricted Three-Body Problem (CR3BP) describes the motion of a body (P_3) with insignificant mass, i.e. a spacecraft, under the gravitational influence of two centrobaric bodies (P_1, P_2) that revolves around a common barycenter. The two primary bodies are assumed to revolve around their barycenter in circular orbits. Due to the negligible mass of P_3, it does not impact the motion of the two primaries and potentially moves in any spatial dimension. The equations of motion of the model are commonly expressed in a rotating frame with $\hat{x}$-axis as the line joining the greater mass primary to the smaller mass primary, $\hat{z}$-axis is defined parallel to the $P_1 - P_2$ orbital angular momentum vector, and $\hat{y}$-axis is along a direction such that the three axes form a dextral orthogonal triad. The equations are non-dimensionalized through three characteristic quantities: (i) sum of the mass of P_1 (m_1) and P_2 (m_2), (ii) distance between $P_1 - P_2$, and (iii) a time quantity that yields a unity non-dimensional value for the gravitational constant. The non-dimensional equations of motion as viewed by an observer in the rotating frame are expressed as,

$$\hat{x} : \ddot{x} - 2\dot{y} - x = -\frac{(1-\mu)(x+\mu)}{r_{13}^3} - \frac{\mu(x-1+\mu)}{r_{23}^3} \tag{1}$$

$$\hat{y} : \ddot{y} + 2\dot{x} - y = -\frac{(1-\mu)y}{r_{13}^3} - \frac{\mu y}{r_{23}^3} \tag{2}$$

$$\hat{z} : \ddot{z} = -\frac{(1-\mu)z}{r_{13}^3} - \frac{\mu z}{r_{23}^3} \tag{3}$$

where, $(x, y, z, \dot{x}, \dot{y}, \dot{z})$ are the position and velocity components of the spacecraft with respect to the $P_1 - P_2$ barycenter, μ is the mass parameter defined as $\frac{m_2}{m_1+m_2}$, and r_{13} and r_{23} denote the distance of the spacecraft from P_1 and P_2, respectively. The equations are time-independent as a result of the choice of the reference frame. There exists no analytical solution to the model, however, particular solutions are determined by leveraging the dynamical systems theory. The equations have three types of particular solutions: stationary, periodic, and quasi-periodic solutions. There are five stationary solutions of CR3BP termed the Lagrange points. The periodic and quasi-periodic solutions exist as families of periodic and quasi-periodic orbits. The particular solutions and their corresponding stable and unstable manifolds assist in defining a part of the global dynamics of the system.

An integral of motion for the system exists and the energy-like quantity is denoted as *Jacobi Constant* (JC). The integration constant is expressed as,

$$JC = 2\left(\frac{x^2+y^2}{2} + \frac{1-\mu}{r_{13}} + \frac{\mu}{r_{23}}\right) - (\dot{x}^2 + \dot{y}^2 + \dot{z}^2) \tag{4}$$

The above expression reveals the bounds for the natural motion of a spacecraft with a specific JC value. The quantity is constant for all the states along a ballistic trajectory. Consequently, two states with the same JC value may be linked by a maneuver-free trajectory.

B. Periodic Orbits

Periodic orbits are fundamental dynamical structures in the CR3BP, characterized by repeating geometries after a finite period, and exist in families characterized by a single parameter. The orbits are described by a single fundamental frequency that is associated with their period. Hence, any state on a periodic orbit is alternatively represented as a single parameter, that is the propagation time (τ_{PO}) along the orbit from an initial state. The 1-parameter families of periodic orbits are constructed via differential corrections and continuation processes, as detailed by Grebow [12]. For instance, fig. 1(a) depicts the L_1 northern halo orbit family generated through such a procedure. The periodic nature of these orbits makes them an attractive choice for mission design.

The periodic orbits often possess unstable and stable manifolds that potentially assist in the construction of transfers between different regions of the space domain. The motion of a periodic orbit and the region surrounding it are characterized by a State Transition Matrix (STM) associated with the CR3BP equations of motion. A special case of an STM that is computed for one period of a periodic orbit state is termed the monodromy matrix. The eigenanalysis of the monodromy matrix reveals the Lyapunov stability of the orbit and assists in the approximation of the corresponding invariant manifolds. The six eigenvalues ($\lambda_i, i \in [1, 6]$) of the monodromy matrix appear as reciprocal pairs due to the symplectic nature of the model. Additionally, one of the three pairs is unity and is labelled the trivial pair [13]. An eigenvalue located away from the unit circle indicates hyperbolic local dynamics, while an eigenvalue that lies on the unit circle signifies bounded motion along a higher-period or higher-dimensional orbit. A stability index is defined to alternatively represent the information offered by the eigenvalues and it is expressed as,

$$\nu_i = \frac{1}{2}(|\lambda_i| + \frac{1}{|\lambda_i|}) \tag{5}$$

Where, ν_i corresponds to the stability index of λ_i. The indices for $i = 1$ and $i = 2$ pertain to the first and second non-trivial eigenvalue pairs, respectively. A value of ν_i equal to one for multiple adjacent orbit family members signals the presence of nearby higher-dimensional orbits. Whereas, a value of ν_i greater than one indicates the existence of associated hyperbolic invariant manifolds. The stability indices for the L_1 halo orbits, as visualized in fig. 1(a), are plotted in fig. 1(b). The center, stable, and unstable invariant manifolds associated with a periodic orbit are locally approximated as a perturbation along the center, stable, and unstable eigenvectors, respectively. The linear approximation of the center manifolds serves as an initial guess for the construction of quasi-periodic orbits. The linear estimation of the stable and unstable invariant manifolds assists in the identification of flows that naturally depart and arrive at the orbit. For a periodic orbit (Γ), the stable ($W^S(\Gamma)$) and unstable ($W^U(\Gamma)$) invariant manifolds are each a *2-dimensional* smooth surface of solutions that are computationally approximated as a collection of stable and unstable manifold arcs. A local unstable manifold state (${}_u\bar{x}^0$) associated with a periodic orbit state ($\bar{x}_{\text{PO}}(\tau_{\text{PO}})$) is approximated as,

$${}_u\bar{x}^0 = \bar{x}_{\text{PO}}(\tau_{\text{PO}}) \pm \nabla_u \frac{\bar{v}_u}{|\bar{v}_u|} \tag{6}$$

where, $\bar{v}_u$ is an unstable eigenvector associated with the $\bar{x}_{\text{PO}}(\tau_{\text{PO}})$ state and ∇_u is a step-off factor that scales the magnitude of the perturbation along the eigenvector. It is apparent that due to two choices of the direction of perturbation in eq. (6), the expression results in two values for the local manifold state, $W^{U^+}_{loc}(\bar{x}_{\text{PO}}(\tau_{\text{PO}}))$ and $W^{U^-}_{loc}(\bar{x}_{\text{PO}}(\tau_{\text{PO}}))$. The local unstable manifold states are propagated forward in time to construct manifold arcs and this procedure is repeated for several periodic orbit states around the orbit with a common ∇_u value. The collection of $W^{U^+}(\bar{x}_{\text{PO}}(\tau_{\text{PO}}))$ and $W^{U^-}(\bar{x}_{\text{PO}}(\tau_{\text{PO}}))$ manifold arcs generated through multiple orbit states deliver an approximation of the two halves of the *2-dimensional* unstable manifold, $W^{U^+}(\Gamma)$ and $W^{U^-}(\Gamma)$. The two half-unstable manifolds combined define the global unstable manifold associated with a periodic orbit. The same strategy is employed but with stable eigenvectors to approximate the two halves of the *2-dimensional* stable manifold, $W^{S^+}(\Gamma)$ and $W^{S^-}(\Gamma)$. The stable and unstable manifolds generated through the described strategy are illustrated for an L_1 halo orbit in fig. 2. The stable and unstable manifolds associated with a periodic orbit may assist in the construction of low maneuver cost pathways towards and away from the orbit.

The Floquet theory provides a powerful framework for analyzing the linear variational dynamics near a periodic orbit [14]. From the theory, an STM between any two states ($\mathbf{\Phi}(\tau, \tau_0)$) on a periodic orbit is decomposed into the following form,

$$\mathbf{\Phi}(\tau, \tau_0) = F(\tau)\text{e}^{B(\tau-\tau_0)}F^{-1}(\tau_0) \tag{7}$$

where, $F(\tau_0)$ denotes a matrix that consists of the eigenvectors of the orbit state at τ_0, B represents a Jordan canonical matrix comprising of the Poincaŕe exponents of the orbit, and $F(\tau)$ signifies a matrix that contains the Floquet modes

associated with a periodic orbit state at τ time downstream from an initial state at τ_0. The Poincaŕe exponents (η_i) are related to the eigenvalues of a periodic orbit with a period ($\mathbb{P}$) as,

$$\eta_i = \frac{1}{\mathbb{P}} \ln(\lambda_i) \tag{8}$$

The $F(\tau_0)$ matrix for a periodic orbit of type saddle x center is written in terms of the eigenvectors as,

$$F(\tau_0) = [\bar{v}_o \ \bar{v}_f \ \bar{v}_u \ \bar{v}_s \ \bar{v}_{c,r} \ \bar{v}_{c,i}] \tag{9}$$

where, the six eigenvectors in the above-presented order correspond to the along orbit, generalized, unstable, stable, real component of the center and imaginary component of the center eigenvector. Since the geometric multiplicity of the trivial eigenvalue pair is one it is challenging to compute the generalized eigenvector. The methodology described by Williams and Howell is leveraged to identify the generalized eigenvector [15]. The associated $e^{B(\tau-\tau_0)}$ matrix for a periodic orbit of type saddle x center is determined as,

$$e^{B(\tau-\tau_0)} = \begin{bmatrix} 1 & \epsilon & 0 & 0 & 0 & 0 \\ 0 & 1 & 0 & 0 & 0 & 0 \\ 0 & 1 & e^{\eta_3(\tau-\tau_0)} & 0 & 0 & 0 \\ 0 & 1 & 0 & e^{-\eta_3(\tau-\tau_0)} & 0 & 0 \\ 0 & 1 & 0 & 0 & \cos(\mathrm{Im}[\eta_5](\tau-\tau_0)) & \sin(\mathrm{Im}[\eta_5](\tau-\tau_0)) \\ 0 & 1 & 0 & 0 & -\sin(\mathrm{Im}[\eta_5](\tau-\tau_0)) & \cos(\mathrm{Im}[\eta_5](\tau-\tau_0)) \end{bmatrix} \tag{10}$$

where, ϵ is an arbitrarily small number, η_3 represents the Poincaŕe exponent related to the unstable eigenvector, and $\mathrm{Im}[\eta_5]$ denotes the imaginary component of the Poincaŕe exponent associated with the complex center eigenvalue. The Floquet modes associated with an orbital state are computed by rearranging the terms in eq. (7) as,

$$F(\tau) = \boldsymbol{\Phi}(\tau, \tau_0) F(\tau_0) e^{-B(\tau-\tau_0)} \tag{11}$$

The six $\mathbb{P}$-periodic Floquet modes offer a convenient representation of the eigenvectors associated with periodic orbits and are employed by multiple authors for the formulation of stationkeeping and transfer design strategies [11, 14, 16].

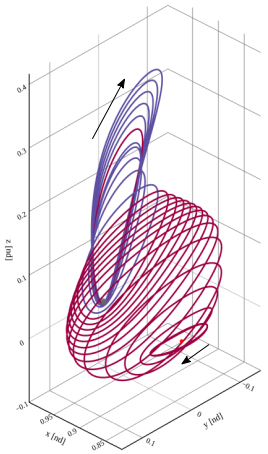

(a) Configuration plot

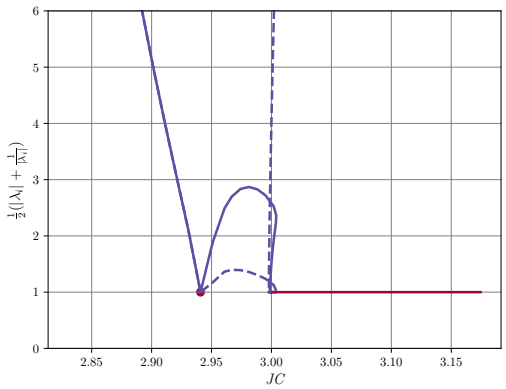

(b) *JC* vs stability index, solid and dash line represent values corresponding to two different eigenvalue pairs

Fig. 1 The L_1 northern halo orbit family members in the Earth-Moon system and stability indices, where crimson: family members with at least one non-trivial *2-dimensional* center subspace

C. Quasi-Periodic Orbits

Quasi-periodic orbits are non-repeatable but bounded particular solutions of the CR3BP that are characterized by n-fundamental frequencies ($n \geq 2$) that are not commensurate. The focus of this investigation is limited to QPOs that are

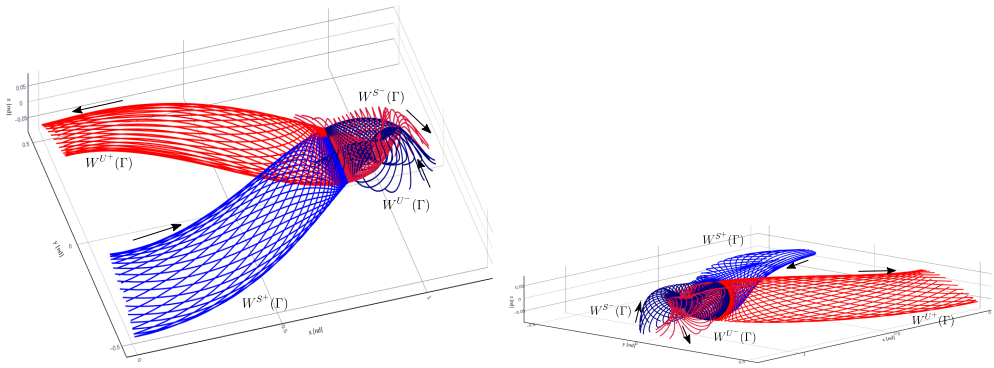

Fig. 2 The stable and unstable global manifolds associated with an L_1 halo orbit

described by two fundamental frequencies. The two key parameters linked to a QPO are the stroboscopic time period (T^0) that defines the time it takes for a trajectory to complete one revolution around a QPO, and the rotation angle (ρ^0) that denotes the latitudinal shift in a quasi-periodic trajectory after every revolution of the orbit. The two fundamental frequencies are related to the stroboscopic time period and the rotation angle through the following expressions,

$$\omega_{T^0} = \frac{2\pi}{T^0} \tag{12}$$

$$\omega_{\rho^0} = \frac{\rho^0}{T^0} = \frac{\rho^0 \omega_{T^0}}{2\pi} \tag{13}$$

where, ω_{T^0} represents the longitudinal frequency and ω_{ρ^0} denots the latitudinal frequency. Since the two fundamental frequencies are constant, any phase state on a QPO is alternatively expressed as a pair of angular variables (θ_{T^0}, θ_{ρ^0}) as depicted in fig. 3. The two angles linearly evolve with the propagation time, τ, from a state ($\theta_{T^0}(0)$, $\theta_{\rho^0}(0)$) on a QPO and they are defined as,

$$\theta_{T^0}(\tau) = \theta_{T^0}(0) + \omega_{T^0}\tau \tag{14}$$

$$\theta_{\rho^0}(\tau) = \theta_{\rho^0}(0) + \omega_{\rho^0}\tau \tag{15}$$

The angular representation is helpful in succinctly describing any phase state on a QPO and has been leveraged to realize various applications by a number of authors [8, 17, 18]. However, the angles as commonly defined do not preserve the information about the natural flow along the orbit, i.e., it is not straightforward to identify if two states on a QPO lie along a common short time of flight (TOF) quasi-periodic trajectory. Hence, the definition of the latitudinal angle is altered such that all the QPO states that lie within one stroboscopic time period downstream of an initial state are represented by the latitudinal angle of the initial state. This new latitudinal angle is denoted as the modified latitudinal angle, Ω_{ρ^0}. It is evident that the Ω_{ρ^0} value for all the states that lie one revolution downstream from an initial state is constant, whereas, the θ_{ρ^0} value for the states evolve as a function of propagation time. For the states that are more than one revolution downstream from an initial state, their Ω_{ρ^0} values are updated by the number of revolutions downstream they lie times the rotation angle. It is straightforward to ascertain if a short TOF quasi-periodic trajectory connects the two states if they either have the same Ω_{ρ^0} value or the difference in their Ω_{ρ^0} values is a small integer multiple of the rotation angle of the QPO. Hence, in this investigation θ_{T^0} and Ω_{ρ^0} are employed to alternatively represent the phase states of a QPO.

A number of characteristics of the flow along a QPO are uncovered by identifying an image of the orbit that crosses through a stroboscopic map with the same time period as the T^0 value of the QPO. The generated image is identified as an invariant curve, and it assists in realizing that an initial state on the curve when propagated till the next crossing of the stroboscopic map does not return to the initial state albeit shifted along the invariant curve by the rotation angle of the QPO. This characteristic is formulated as an invariance constraint for a differential corrections scheme to construct QPOs and it was first proposed by Gómez and Mondelo [19], and later refined by Olikara and Scheeres [20]. Specifically, the differential corrections scheme described by Olikara and Scheeres termed the GMOS algorithm is employed in this investigation [20]. The initial guess for an invariant curve is delivered by the approximation of the center manifold

associated with a periodic orbit state through the following expression,

$$\bar{x}_c^* = \bar{x}_{\text{PO}}^* + \nabla \frac{(\text{Re}[\bar{v}_c]\cos(\theta_{\rho^0}) - \text{Im}[\bar{v}_c]\sin(\theta_{\rho^0}))}{\sqrt{v_{c,x}^2 + v_{c,y}^2 + v_{c,z}^2}} \tag{16}$$

Where, $\bar{x}_{\text{PO}}^*$ represents a state on the periodic orbit, ∇ denotes the step-off distance from the periodic orbit state (measured in unit length), $\bar{v}_c$ signifies the complex center eigenvector associated with $\bar{x}_{\text{PO}}^*$ and $\text{Re}[\bar{v}_c]$ and $\text{Im}[\bar{v}_c]$ are the real and imaginary components of the eigenvector, and θ_{ρ^0} is an arbitrary latitudinal angle $\in [0, 2\pi)$. The eq. (16) is utilized to compute N states and they collectively approximate the invariant curve. The N states are computed for a fixed ∇ value but for different latitudinal angles given as,

$$\bar{\theta}_{\rho^0} = \begin{bmatrix} 0 & \frac{2\pi}{N} & \dots & \frac{2\pi(N-2)}{N} & \frac{2\pi(N-1)}{N} \end{bmatrix};\ \theta_{\rho^0,i} = \frac{2\pi(i-1)}{N}, i = 1, 2, \dots, N \tag{17}$$

The basepoint of the N states is modified from the barycenter of the system to the selected periodic orbit state as,

$$\bar{u}_i^1 = \bar{x}^*_{c,\theta_{\rho^0,i}} - \bar{x}_{\text{PO}}^*,\ i \in [1, N] \tag{18}$$

where, $\bar{u}_i^1 = [u^1_{x,i}\ u^1_{y,i}\ u^1_{z,i}\ u^1_{\dot{x},i}\ u^1_{\dot{x},i}\ u^1_{\dot{z},i}]^T$ represents the i^{th} state on the invariant curve. To differentially correct the initial guess the following representation of the invariance constraint is leveraged,

$$(\mathbf{R}_{-\rho^0})(^{\mathbf{T^0}}\mathbf{U}) - \mathbf{U} = 0 \tag{19}$$

where, $\mathbf{U}$ is a matrix that comprises of the $\bar{u}_i^1$ states, $^{\mathbf{T^0}}\mathbf{U}$ is defined in a similar manner as $\mathbf{U}$ but comprises of states that are computed by propagating the $\bar{u}_i^1$ states for one T^0 value, and $\mathbf{R}_{-\rho^0}$ signifies a rotation operator that removes the ρ^0 rotation of the propagated states, so that the corrected propagated states after the $-\rho^0$ rotation match the initial states. The expanded form of the $^{T^0}\mathbf{U}$ matrix is written as,

$$^{\mathbf{T_0}}\mathbf{U} = \begin{bmatrix} {}^{T_0}\bar{u}_1^{1T} \\ {}^{T_0}\bar{u}_2^{1T} \\ \vdots \\ {}^{T_0}\bar{u}_{N-1}^{1T} \\ {}^{T_0}\bar{u}_N^{1T} \end{bmatrix} = \begin{bmatrix} {}^{T_0}u^1_{x,1} & {}^{T_0}u^1_{y,1} & {}^{T_0}u^1_{z,1} & {}^{T_0}u^1_{\dot{x},1} & {}^{T_0}u^1_{\dot{y},1} & {}^{T_0}u^1_{\dot{z},1} \\ {}^{T_0}u^1_{x,2} & {}^{T_0}u^1_{y,2} & {}^{T_0}u^1_{z,2} & {}^{T_0}u^1_{\dot{x},2} & {}^{T_0}u^1_{\dot{y},2} & {}^{T_0}u^1_{\dot{z},2} \\ \vdots & \vdots & \vdots & \vdots & \vdots & \vdots \\ {}^{T_0}u^1_{x,N-1} & {}^{T_0}u^1_{y,N-1} & {}^{T_0}u^1_{z,N-1} & {}^{T_0}u^1_{\dot{x},N-1} & {}^{T_0}u^1_{\dot{y},N-1} & {}^{T_0}u^1_{\dot{z},N-1} \\ {}^{T_0}u^1_{x,N} & {}^{T_0}u^1_{y,N} & {}^{T_0}u^1_{z,N} & {}^{T_0}u^1_{\dot{x},N} & {}^{T_0}u^1_{\dot{y},N} & {}^{T_0}u^1_{\dot{z},N} \end{bmatrix} \tag{20}$$

where, ${}^{T_0}\bar{u}_i^1$ denote the states that lie one stroboscopic time period downstream from the $\bar{u}_i^1$ states. The $\mathbf{U}$ matrix is shaped in the same manner as the $^{T^0}\mathbf{U}$ matrix represented in eq. (20). The rotation operator, $\mathbf{R}_{-\rho^0}$, is constructed via the discrete Fourier series representation of the states that approximate the invariant curve. The Fourier coefficients corresponding to the ${}^{T_0}\bar{u}_i^1$ states are phase-shifted by $-\rho^0$ and the resultant coefficients are transformed to the phase space to deliver the rotation operator. The discrete Fourier coefficients, $^{\mathbf{T_0}}\mathbf{C_0}$, associated with the ${}^{T_0}\bar{u}_i^1$ states are determined as,

$$^{T_0}\mathbf{C}_0 = (\mathbf{D})(^{\mathbf{T_0}}\mathbf{U}) \tag{21}$$

where, $\mathbf{D}$ represents the discrete Fourier transform and is defined as,

$$\mathbf{D} = \frac{1}{N} e^{-i\bar{k}^T \bar{\theta}_{\rho^0}} \tag{22}$$

$$= \frac{1}{N} \begin{bmatrix} e^{-i(-\frac{N-1}{2})0} & e^{-i(-\frac{N-1}{2})\frac{2\pi}{N}} & \dots & e^{-i(-\frac{N-1}{2})\frac{2\pi(N-1)}{N}} \\ \vdots & \vdots & & \vdots \\ e^{-i(-1)0} & e^{-i(-1)\frac{2\pi}{N}} & \dots & e^{-i(-1)\frac{2\pi(N-1)}{N}} \\ e^{-i(0)0} & e^{-i(0)\frac{2\pi}{N}} & \dots & e^{-i(0)\frac{2\pi(N-1)}{N}} \\ e^{-i(1)0} & e^{-i(1)\frac{2\pi}{N}} & \dots & e^{-i(1)\frac{2\pi(N-1)}{N}} \\ \vdots & \vdots & & \vdots \\ e^{-i(\frac{N-1}{2})0} & e^{-i(\frac{N-1}{2})\frac{2\pi}{N}} & \dots & e^{-i(\frac{N-1}{2})\frac{2\pi(N-1)}{N}} \end{bmatrix} \tag{23}$$

The $\bar{\theta}_{\rho^0}$ values are given by eq. (17) and the $\bar{k}$ for odd-valued N is written as,

$$\bar{k} = \left[-\frac{N-1}{2} \quad \dots \quad -1 \quad 0 \quad 1 \quad \dots \quad \frac{N-1}{2} \right] \tag{24}$$

The Fourier coefficients are phase-shifted through a phase-shift operator that adds the desired change in phase to the phase of the coefficients. The phase-shift operator to accomplish a phase change of $-\rho^0$ value is expressed as,

$$\mathbf{Q}_{-\rho^0} = \mathrm{e}^{-\mathrm{i}\bar{k}\rho^0}\mathbf{I}_{N\times N} = \begin{bmatrix} \mathrm{e}^{\mathrm{i}(-\frac{N-1}{2})-\rho^0} & 0 & \dots & 0 \\ 0 & \mathrm{e}^{\mathrm{i}(-\frac{N-1}{2}+1)-\rho^0} & \dots & 0 \\ \vdots & \vdots & \ddots & \vdots \\ 0 & 0 & \dots & \mathrm{e}^{\mathrm{i}(\frac{N-1}{2})-\rho^0} \end{bmatrix} \tag{25}$$

where, $\mathbf{I}_{N\times N}$ is the identity matrix of size $N \times N$. The outlined discrete Fourier transform and the phase-shift operator are combined to define the rotation operator as,

$$(\mathbf{R}_{-\rho^0})(^{\mathbf{T^0}}\mathbf{U}) = (\mathbf{D}^{-1}\mathbf{Q}_{-\rho^0}\mathbf{D})(^{\mathbf{T^0}}\mathbf{U}) \tag{26}$$

The details behind the construction of design and constraint vectors, Jacobian matrix and other considerations for the GMOS algorithm are elucidated by McCarthy [8] and Jain [21]. The *2-dimensional* QPOs exist in *2-parameter* families of orbits. The biparametric family of a QPO is decomposed into three subsets: constant mapping time, constant frequency ratio, and constant energy family that comprises of QPOs with common T^0, ρ^0, and JC values, respectively, as depicted in fig. 4. The three subsets of the biparametric family are constructed through the GMOS algorithm [8, 20, 21] and a constant energy family of L_4 quasi-axials orbits generated through the algorithm is illustrated in fig. 5. The constant energy families of QPOs are extensively employed in this investigation to design transfer pathways.

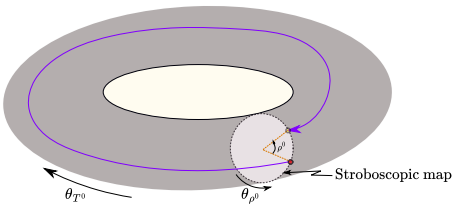

Fig. 3 Phase states on a QPO defined by θ_{T^0} and θ_{ρ^0} angles.

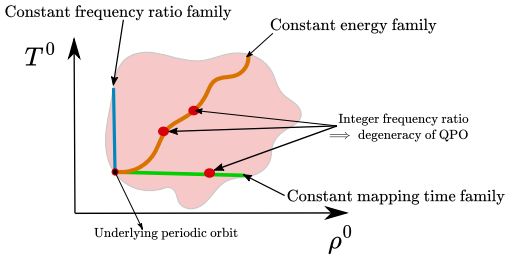

Fig. 4 Schematic of a *2-dimensional* solution surface representing the biparametric family of QPOs.

The stable and unstable manifolds associated with QPOs assist in the identification of transfer pathways. The Lyapunov stability and a first-order linear approximation of the hyperbolic invariant manifolds corresponding to a QPO are determined through the eigenanalysis of a monodromy-like matrix. The matrix akin to the monodromy matrix renders a state on the QPO as a fixed point and the matrix is evaluated as,

$$\mathbf{DG}_{\mathrm{qpo}} = (\mathbf{R}_{-\rho^0} \otimes \mathbf{I})\tilde{\mathbf{\Phi}}(T^0, 0) \tag{27}$$

where, $\mathbf{R}_{-\rho^0}$ is the rotation operator as mentioned in eq. (19), $\otimes$ signifies the Kronecker delta product, $\mathbf{I}$ denotes an identity matrix of size 6×6, and $\tilde{\mathbf{\Phi}}(T^0, 0)$ represents a block diagonal matrix comprising of STMs of the ${}^{T_0}\bar{u}_i^1$ states with respect to the $\bar{u}_i^1$ states. The eigenvalues, $\underbrace{\lambda}$, of the $\mathbf{DG}_{\mathrm{qpo}}$ matrix, size $6N \times 6N$, assist in assessing the Lyapunov stability of the orbit. The $6N$ eigenvalues when plotted on a complex plane appear as six concentric circles as depicted for an L_1 quasi-lyapunov orbit in fig. 6. It is evident that the $6N$ eigenvalues are reducible to six values corresponding to the radius of the concentric circles, and are also described by the six eigenvalues of a Floquet matrix representation of $\mathbf{DG}_{\mathrm{qpo}}$ as outlined by Jorba [22], Baresi et al. [23], and McCarthy [8]. The six Floquet matrix eigenvalues are approximated as positive real eigenvalues with no imaginary component along each concentric circle. The reduced eigenvalues exist as reciprocal pairs, similar to that of a periodic orbit. Two pairs of eigenvalues are unity, and the third

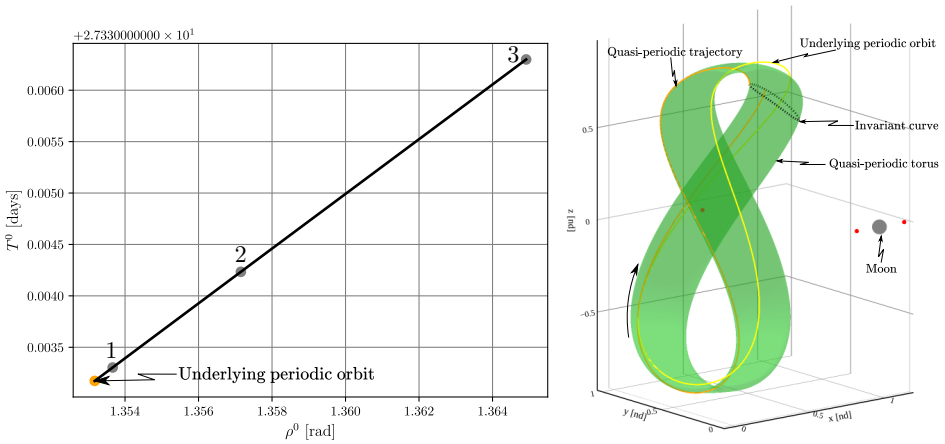

(a) T^0 vs ρ^0 **(b) Congiguration space plot of 3**

Fig. 5 T^0 vs ρ^0 plot of a constant energy family of QPOs with JC_{avg}=1.97268 originating from an L_4 axial orbit (JC=1.97268, T^0=27.33317 days) in the Earth-Moon system. A QPO identified as 3 in the T^0 vs ρ^0 plot is visualized in the configuration space on the right.

pair, if hyperbolic, suggests the presence of associated stable and unstable manifolds. The stable and unstable manifolds corresponding to a QPO are *3-dimensional* and are approximated via the $6N$ stable and unstable eigenvectors associated with the reduced hyperbolic eigenvalue pair. The pair of eigenvectors are expressed as,

$$ {}_{\text{qpo}}\bar{v}_S = \begin{bmatrix} {}_{\text{qpo}}\bar{v}_{S,1} \\ {}_{\text{qpo}}\bar{v}_{S,2} \\ \vdots \\ {}_{\text{qpo}}\bar{v}_{S,N-1} \\ {}_{\text{qpo}}\bar{v}_{S,N} \end{bmatrix}; \quad {}_{\text{qpo}}\bar{v}_U = \begin{bmatrix} {}_{\text{qpo}}\bar{v}_{U,1} \\ {}_{\text{qpo}}\bar{v}_{U,2} \\ \vdots \\ {}_{\text{qpo}}\bar{v}_{U,N-1} \\ {}_{\text{qpo}}\bar{v}_{U,N} \end{bmatrix} \tag{28} $$

where, ${}_{\text{qpo}}\bar{v}_S$ and ${}_{\text{qpo}}\bar{v}_U$ represent the $6N$ stable and unstable eigenvectors, repectively, and ${}_{\text{qpo}}\bar{v}_{S,i}$ and ${}_{\text{qpo}}\bar{v}_{U,i}$ signify the stable and unstable eigenvector associated with the $\bar{u}_i^1$ state. The local stable and unstable manifolds associated with an invariant curve, sampled using $\bar{u}^1$ states, are approximated as,

$$ {}_{\text{qpo}}\bar{x}^*_{S,i} = \bar{x}^*_{\text{PO}} + \bar{u}_i^1 \pm \nabla \frac{{}_{\text{qpo}}\bar{v}_{S,i}}{\sqrt{{}_{\text{qpo}}v^2_{S,i,x} + {}_{\text{qpo}}v^2_{S,i,y} + {}_{\text{qpo}}v^2_{S,i,z}}} \tag{29} $$

$$ {}_{\text{qpo}}\bar{x}^*_{U,i} = \bar{x}^*_{\text{PO}} + \bar{u}_i^1 \pm \nabla \frac{{}_{\text{qpo}}\bar{v}_{U,i}}{\sqrt{{}_{\text{qpo}}v^2_{U,i,x} + {}_{\text{qpo}}v^2_{U,i,y} + {}_{\text{qpo}}v^2_{U,i,z}}} \tag{30} $$

where, ${}_{\text{qpo}}\bar{x}^*_{S,i}$ and ${}_{\text{qpo}}\bar{x}^*_{U,i}$ denote the local stable and unstable manifold approximation associated with the $\bar{u}_i^1$ state, and ∇ denotes a step-off factor with length units. This procedure is repeated to approximate the local hyperbolic manifold states corresponding to other invariant curves around the torus. The collection of local unstable manifold states linked to various invariant curves, serves as an estimate of the local unstable manifold associated with a QPO. Then, the *3-dimensional* unstable manifold is approximated as the set of the unstable manifold arcs that are generated by flowing the local unstable manifold states forward in time. The same methodology is followed to compute local stable manifold states to estimate the stable manifold. The positive-half unstable manifold approximated through the described technique is plotted for an L_2 quasi-vertical orbit in fig. 7. Since, the stable and unstable manifolds are *3-dimensional*, any state on the manifold may be parameterized as the step-off location (θ_{T^0}, Ω_{ρ^0}) of its corresponding manifold arc and the propagation time along the manifold arc from the approximated local manifold state to the desired state. The stable and unstable manifolds inform the design of transfer pathways towards and away from a QPO.

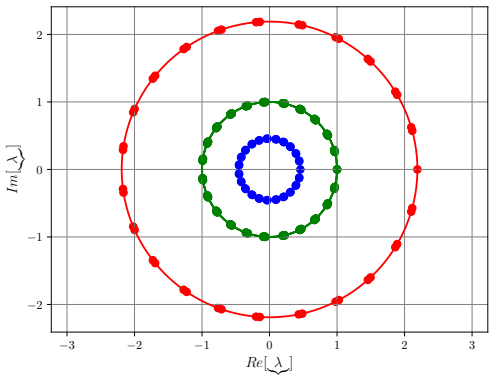

Fig. 6 The spectrum of eigenvalues of DG_{qpo} of an L_1 quasi-Lyapunov orbit.

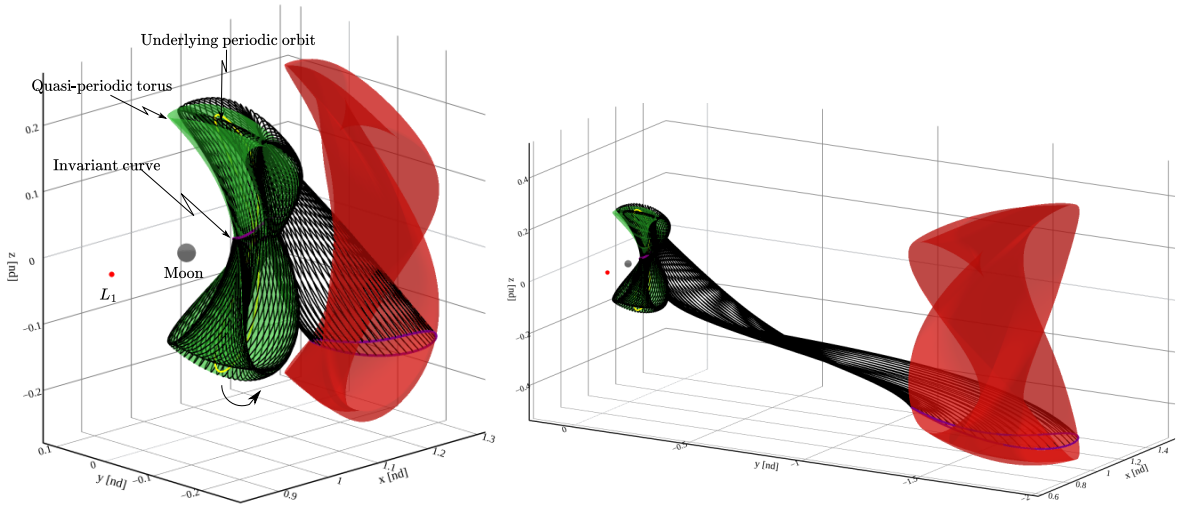

(a) **(b)**

Fig. 7 Approximation of positive-half unstable manifold associated with an L_2 quasi-vertical orbit(green) (JC_{avg} = 3.04647, T^0 = 16.82590 days) in the Earth-Moon system. The global unstable manifold trajectories (black) associated with N = 55 states, for ∇_u = 50 km, emanating from an invariant curve (purple) are depicted in the plots. Additionally, the surface of manifold states (red) generated at 19.95786 days, and 30.39736 days along the manifold are visualized in figs. 7(a) and 7(b), respectively.

III. Transfers Between Stable Periodic Orbits

The construction of transfers between nearly/marginally stable periodic orbits is challenging due to the absence of useful natural flows that depart and arrive at the orbits. The pathways that link two orbits with a reasonable flight time may necessitate costly maneuvers to overcome inherent difference in their geometry and compensate for the lack of practical stable/unstable hyperbolic invariant manifolds. A sample case for this problem is the design of a transfer from an L_2 9:2 synodic resonant southern Near Rectilinear Halo Orbit (NRHO) to a moon-centered planar Distant Retrograde Orbit (DRO), as illustrated in fig. 8. In this scenario, a DRO at the same energy level as the NRHO is chosen as the arrival orbit. The L_2 9:2 NRHO is nearly stable, and the selected DRO is marginally stable, as indicated by the stability indices provided in table 1. A common metric to approximate the lowest transfer cost between two orbits is the theoretical minimum ΔV (TMDV) [24]. The metric assumes that the orbits possess natural flows linked by a single impulsive maneuver, resulting in a ΔV of 0 m/s for the two selected orbits at the same energy level. However, the absence of stable/unstable manifolds associated with the DRO necessitates an insertion maneuver. This scenario motivates the use of at least one other dynamical structure to inform the transfer design process.

For the sample case of a general NRHO to DRO scenario, multiple solutions have been constructed by several

Table 1 Initial conditions, period, JC value and stability indices of an L_2 9:2 southern NRHO and a DRO.

Orbit	x_0 [nd]	z_0 [nd]	$\dot{y}_0$ [nd]	$\mathbb{P}$ [nd]	JC	ν_1	ν_2
L_2 9:2 southern NRHO	1.02203	-0.18210	-0.10327	1.51120	3.04649	1	1.32301
DRO	0.91009	0	0.48639	1.08309	3.04649	1	1

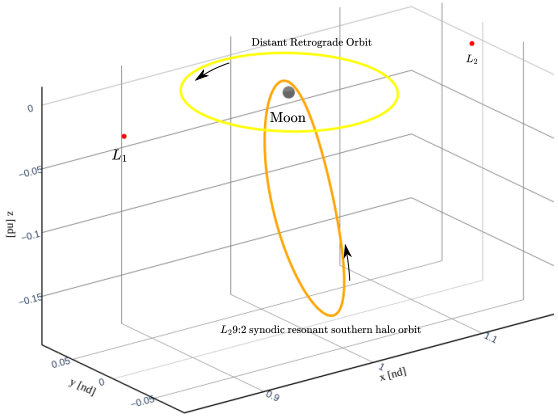

Fig. 8 An L_2 9:2 NRHO (orange) and a DRO (yellow) in the Earth-Moon system.

authors. McCarty et al. use monotonic basin hopping to locate a feasible exterior transfer, such that the transfer traverses the far side of the Earth [25]. Lantoine considers a patched model approach that incorporates the solar perturbation, DPO family, and a grid search to produce exterior-type transfer geometries [26]. Vutukuri utilizes resonant periodic orbits and tangential maneuvers for recognition of exterior-type transfers [27]. Pritchett et al. and Prado et al. develop interior-type transfer solutions using low-thrust in the periodic orbit chaining process [28, 29]. Zimovan-Spreen et al. compute interior-type transfer pathways by orbit chaining higher-period L_2 halo orbits and their associated manifolds, as well as exterior-type solutions by including resonant orbits in the orbit chain [30]. In addition, Muralidharan and Howell leverage stretching directions corresponding to the departure and arrival orbits to constrain the computation of interior and exterior type class of solutions [31]. The various strategies rely on different dynamical structures to influence the result, so an approach is proposed where the hyperbolic invariant manifolds corresponding to intermediate periodic/quasi-periodic orbits are leveraged to inform the design of transfers.

The formulated methodology leverages the natural flow, as well as stable and unstable manifolds associated with intermediate orbits to uncover two types of transfers: interior-type and exterior-type transfers. The interior-type transfers lie in the interior region of the system and the exterior-type transfers traverse through the far-side of the Earth as depicted in figs. 9 and 10. Both types of transfers require a departure and an arrival impulsive maneuver, and the exterior-type transfers employ an additional impulsive maneuver on the far-side of the Earth. The construction of the transfers is decomposed into the design of three/six segments for interior-type/exterior-type transfers that are informed by the stable and unstable manifolds associated with one/two selected intermediate orbits. The segments that depart and arrive at an intermediate orbit are constructed independent of each other and the two segments are linked by a bridging arc. The design of a bridging arc is informed by the natural flow along a selected intermediate orbit. The various segments are stitched together through a differential corrections scheme to result in two/three maneuver interior-type/exterior-type solutions. Additionally, locally fuel-optimal solutions for the two types of transfers are identified by employing an interior-point method.

The intermediate orbits are selected to possess the same JC value as the departure and arrival orbits, as well as useful stable and unstable invariant manifolds. This criterion aids in reducing the dimensionality of the problem, and the associated maneuvers are solely required to accomplish geometry change and not expended on energy change. The intermediate orbits employed in this investigation to demonstrate the framework include L_2 vertical, L_2 quasi-vertical, L_2 P2HO$_2$, and L_2 quasi-P2HO$_2$ orbits. Additionally, a planar 3:4 sidereal Resonant Periodic Orbit (RPO) and a Distant Prograde Orbit (DPO) are utilized as the second intermediate orbit for the construction of exterior-type transfers as represented in fig. 10. Due to the simplifying assumption associated with the JC value of the intermediate orbits, the orbits of interest offered by a *2-parameter* family of a QPO narrows down to a *1-parameter* constant energy family

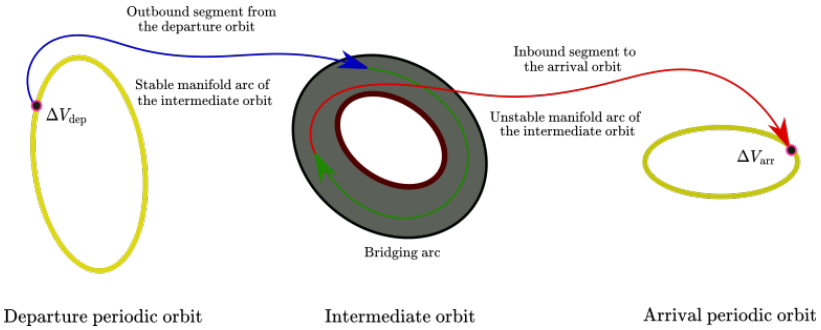

Fig. 9 Interior-type transfer schematic.

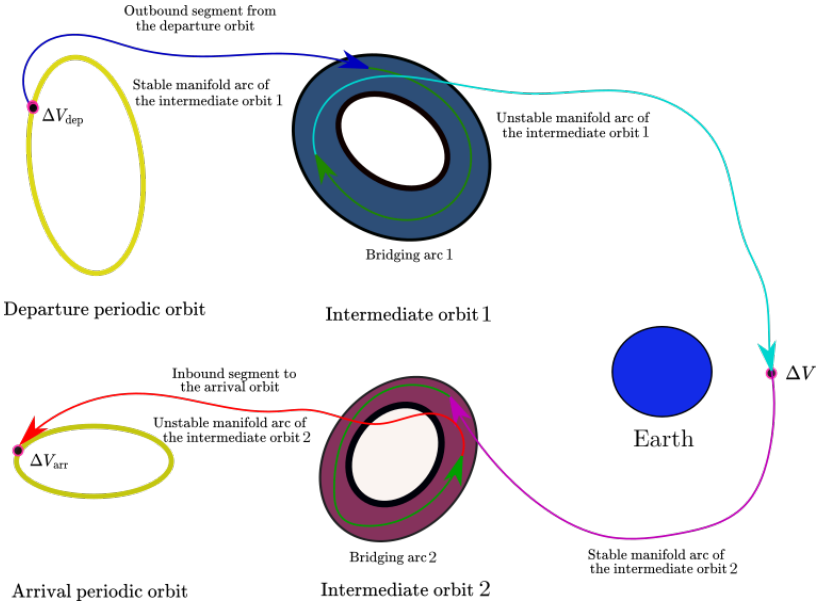

Fig. 10 Exterior-type transfer schematic.

at the same energy level as the departure/arrival orbit. Consequently, the *5-dimensional* solutions encompassed by the stable/unstable manifolds associated with the *2-parameter* family of a QPO reduce to *4-dimensional* solutions corresponding to stable/unstable manifolds of a constant energy family. The relevant characteristics of the selected intermediate periodic orbits appear in table 2, and the orbits are visualized in fig. 11. The characteristics of the constant energy family of L_2 quasi-vertical and L_2 quasi-P2HO$_2$ orbits, at the same JC value as the departure/arrival orbit, employed in this investigation are depicted in figs. 12 and 13, respectively. It is notable that the evolution of the QPOs along the two selected constant energy families is marked by the monotonic decrease in their associated rotation angle. The subsequent sections provide a systematic framework for the computation of the multiple segments of the two transfer types, as well as strategies to link the segments to generate transfers. The various selected intermediate orbits assist in assessing a number of solution basins that exist for the sample case, as well as allow for comparison between geometries constructed via QPOs and their underlying periodic orbits.

A. Inbound Segment to the Arrival Orbit

The inbound segment to the arrival periodic orbit from an intermediate orbit is constructed to lie on the unstable manifold associated with the intermediate orbit. The design of the segment is initiated by identifying unstable manifold arcs that cross the vicinity of the arrival orbit. The potential candidates of the segment are differentially corrected such that the converged trajectory lies on the unstable manifold corresponding to the intermediate orbit and is position continuous with an arrival orbit state. To narrow down the solutions offered by the *1-parameter* constant energy family

Table 2 Initial conditions, period, JC value, and stability indices of the selected intermediate periodic orbits.

Orbit	x_0 [nd]	z_0 [nd]	$\dot{y}_0$ [nd]	$\mathbb{P}$ [nd]	JC	ν_1	ν_2
L_2 vertical	1.05442	-0.19361	0.08128	3.87705	3.04649	1	303.83937
L_2 southern P2HO$_2$	1.02578	0.059137	0.50201	4.20255	3.04649	1	45.64766
Planar 3:4 RPO	0.97615	0	1.40837	16.86499	3.04649	1	228.36123
DPO	1.02731	0	0.72419	4.50999	3.04649	1	619.95934

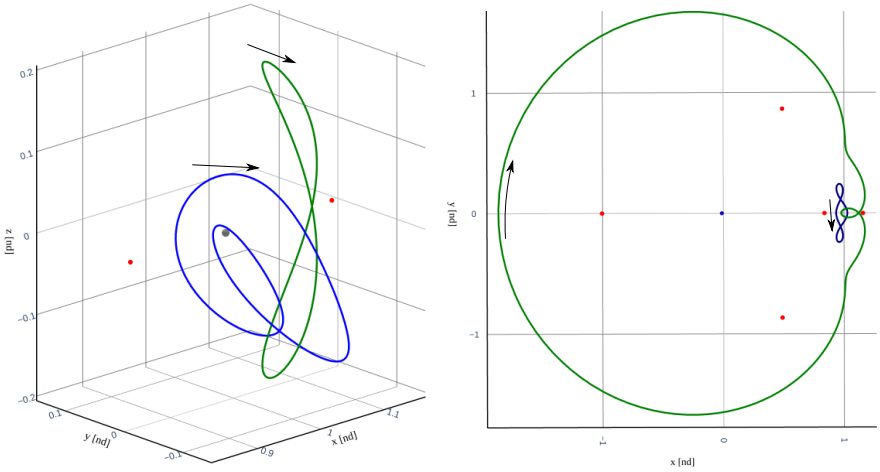

(a) An L_2 vertical (green) and an L_2 P2HO$_2$ (navy). **(b) A planar 3:4 RPO (green) and a DPO (navy).**

Fig. 11 Selected intermediate periodic orbits with the same JC value as an L_2 9:2 NRHO (JC = 3.04649).

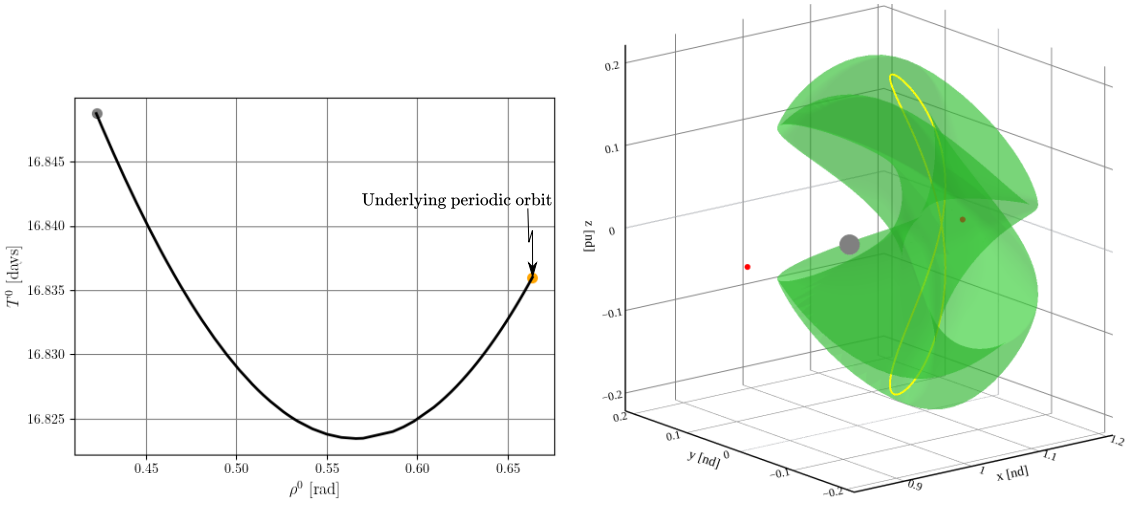

Fig. 12 A constant energy family of L_2 quasi-vertical orbits with the same JC value as an L_2 9:2 NRHO (JC = 3.04649). Plot of the evolution of ρ^0 and T^0 values of the QPOs along the family, and a member (green) with ρ^0 = 0.42259 rad along its the underlying periodic orbit (yellow).

of an intermediate QPO, a representative member of the family is selected that delivers significantly different geometries than derived from its underlying periodic orbit. The initial guesses generated by various members of the constant energy family are compared through a visualization technique to identify a candidate intermediate QPO. The differentially

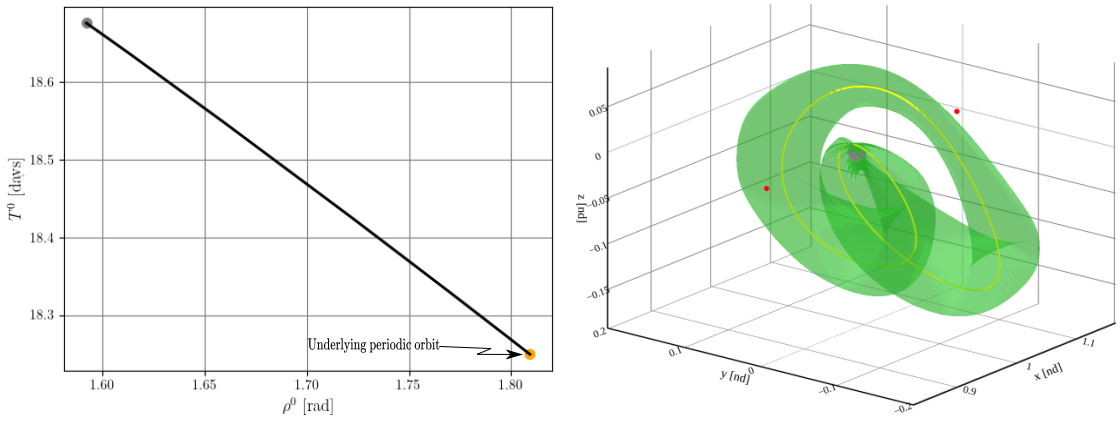

Fig. 13 A constant energy family of L_2 quasi-P2HO$_2$ orbits with the same JC value as an L_2 9:2 NRHO (JC = 3.04649). Plot of the evolution of ρ^0 and T^0 values of the QPOs along the family, and a member (green) with ρ^0 = 1.59184 rad along its the underlying periodic orbit (yellow).

corrected segments constructed through the unstable manifolds associated with intermediate periodic and quasi-periodic orbits exist as locally unique and local *1-parameter* family of solutions due to the dimensionality of their manifolds.

1. Initial Guess

The initial guess for the segment is obtained by recording the first crossings of the unstable manifold arcs near the arrival periodic orbit. The unstable manifold associated with an intermediate periodic/quasi-periodic orbit is approximated through the technique detailed in section II.B/section II.C. To identify the first crossings of the manifold arcs, an events function is leveraged that employs a continuous representation of the DRO constructed through the strategy described by Jain [21]. The manifold states with a position discontinuity of less than 4000 km and a velocity discontinuity of at most 700 m/s are considered. The initial guesses realized through the aforementioned procedure are demonstrated for an L_2 vertical orbit and L_2 quasi-vertical orbits. The manifold arcs and manifold states associated with the L_2 vertical orbit that cross in the proximity of the DRO are visualized in fig. 14. It is apparent from the plot that there are three local solution basins. Similarly, the manifold states of interest corresponding to the L_2 quasi-vertical orbit with ρ_0=0.42259 rad are depicted in fig. 15. Notably, the QPO offers many more solutions than its underlying periodic orbit. The difference in the number of initial guesses generated by intermediate periodic orbit and QPO are a result of the difference in their unstable manifold dimensionality.

To assess the initial guess generated through an intermediate QPO and to compare the guesses derived from the various members of its constant energy family, an alternative visualization technique to fig. 15 is employed. The proposed visualization method represents the identified manifold states on a *2-dimensional* heat map with the two axes as the modified latitudinal angle (Ω_{ρ^0}) and the longitudinal angle (θ_{T^0}), as described in section II.C, associated with the manifold step-off location on the QPO. The manifold states are colored by the position and velocity discontinuity with their nearest arrival orbit states. The heat map representation of the manifold states in fig. 15 associated with the L_2 quasi-vertical orbit with ρ_0=0.42259 rad is depicted in fig. 16. The heat map visual offers a more straightforward method to assess the initial guess than the plot in fig. 15. The outlined initial guess generation and visualization strategies are employed to compare the initial guesses obtained from the other members of the L_2 quasi-vertical constant energy family. The heat map representation of the guesses generated by a number of L_2 quasi-vertical orbits with ρ^0 = 0.51490, 0.60913 and 0.64859 rad are presented in figs. 17 to 19, respectively. It is apparent from figs. 16 to 19 that there is a smooth decrease in velocity discontinuities as the L_2 quasi-vertical orbits evolve along their constant energy family, marked by the decrease in their associated rotation angle. The decrease in the velocity discontinuities is indicative of the change in the manifold arc geometries. Consequently, the quasi-vertical orbit with the smallest rotation angle (ρ^0 = 0.42259 rad), plotted in fig. 12, amongst the constructed constant energy family members is employed for the construction of the segment. Subsequently, the initial guesses marked by the black and red curves in fig. 16 are selected to construct low maneuver cost *1-parameter* families of solutions.

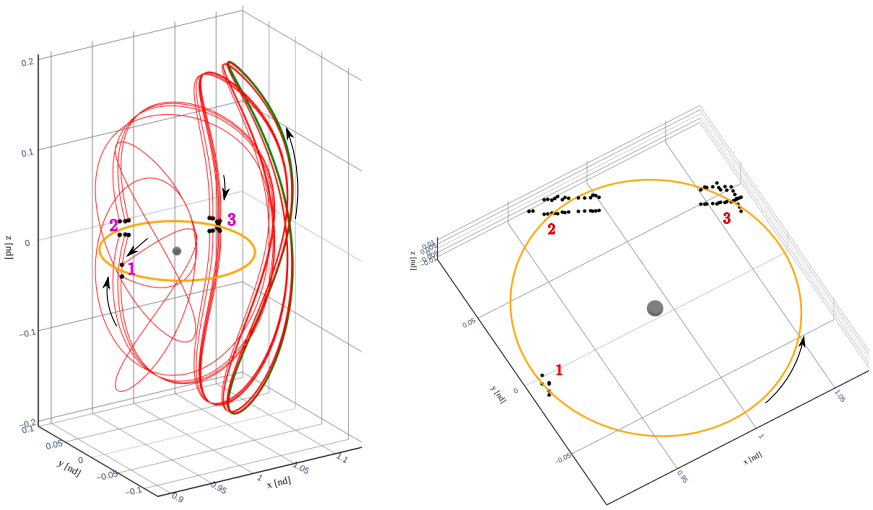

Fig. 14 Unstable manifold arcs (red) on the left and manifold states (black) on the right associated with an L_2 vertical orbit (green) that crosses near a DRO (orange).

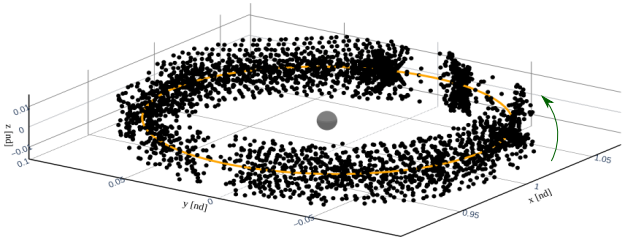

Fig. 15 Unstable manifold states (black) associated with an L_2 quasi-vertical orbit (ρ^0 = 0.42259 rad) that cross near a DRO (orange).

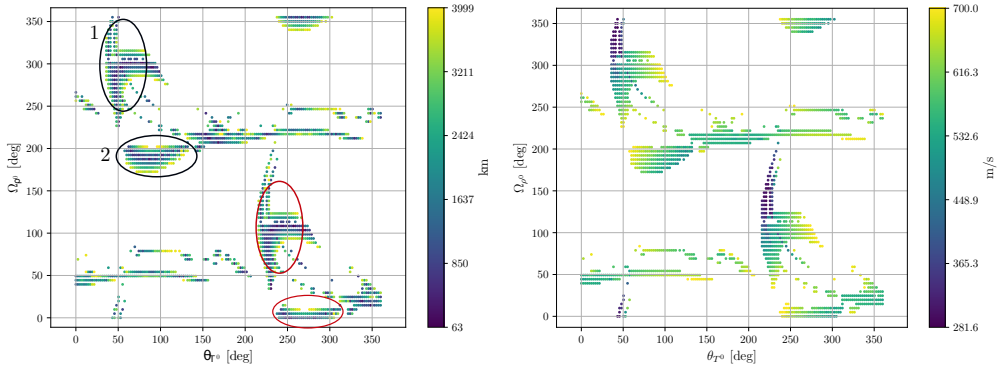

(a) Position discontinuity **(b) Velocity discontinuity**

Fig. 16 Position and velocity discontinuities between the unstable manifold states associated with an L_2 quasi-vertical orbit (ρ^0 = 0.42259 rad) and their corresponding nearest arrival orbit states.

2. Differential Correction

A differential corrections strategy is leveraged to correct an identified initial guess such that the resultant geometry is an unstable manifold arc associated with a selected intermediate orbit and position continuous with an arrival orbit state. Consequently, the velocity discontinuity with the arrival orbit state is overcome through a single impulsive maneuver. The time of flight and the step-off location of a manifold arc on the intermediate orbit, as well as the arrival orbit

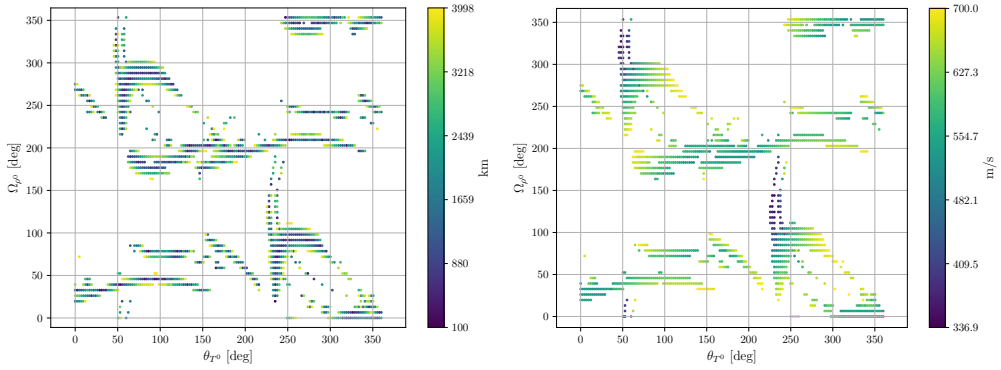

(a) Position discontinuity **(b) Velocity discontinuity**

Fig. 17 Position and velocity discontinuities between the manifold states corresponding with an L_2 quasi-vertical orbit (ρ^0 = 0.51490 rad) and their corresponding nearest arrival orbit states.

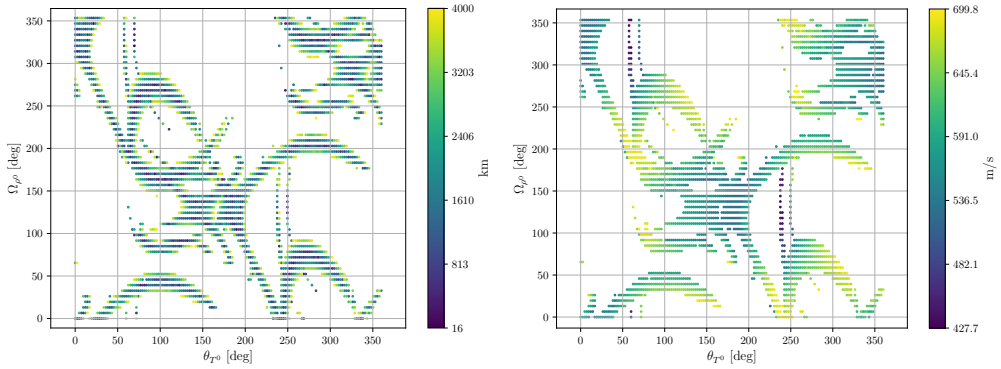

(a) Position discontinuity **(b) Velocity discontinuity**

Fig. 18 Position and velocity discontinuities between the manifold states corresponding with an L_2 quasi-vertical orbit (ρ^0 = 0.60913 rad) and their corresponding nearest arrival orbit states.

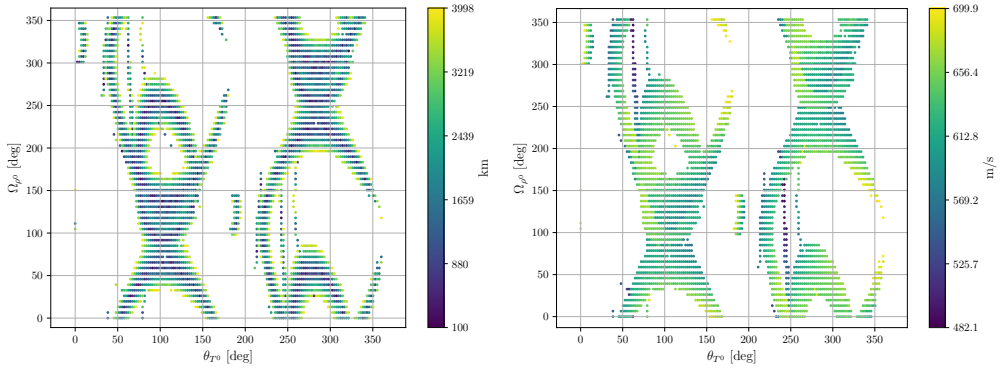

(a) Position discontinuity **(b) Velocity discontinuity**

Fig. 19 Position and velocity discontinuities between the manifold states corresponding with an L_2 quasi-vertical orbit (ρ^0 = 0.64859 rad) and their corresponding nearest arrival orbit states.

state, are allowed to vary during the corrections process. The differential corrections procedure is formulated as a Newton-Raphson method. The design ($\bar{X}$) and constraint vectors ($\bar{F}(\bar{X})$) for solutions derived from an intermediate

QPO are formulated as,

$$\bar{X} = \begin{bmatrix} \mathbb{T} \\ \tau_{\text{arr}} \\ \tau_{\text{int}} \\ \Omega_{\rho^0} \end{bmatrix}; \quad \bar{F}(\bar{X}) = \begin{bmatrix} {}_u x^{\mathbb{T}}_{\tau_{\text{int}},\Omega_{\rho^0}} - x^{\tau_{\text{arr}}}_{\text{arr}} \\ {}_u y^{\mathbb{T}}_{\tau_{\text{int}},\Omega_{\rho^0}} - y^{\tau_{\text{arr}}}_{\text{arr}} \\ {}_u z^{\mathbb{T}}_{\tau_{\text{int}},\Omega_{\rho^0}} - z^{\tau_{\text{arr}}}_{\text{arr}} \end{bmatrix} \tag{31}$$

where, $\mathbb{T}$ corresponds to the time of flight of a manifold arc and τ_{arr} represents the propagation time along the arrival periodic obit from an initial state, $\bar{x}_{\text{arr}}$, on the orbit. The last two elements of the design vector, τ_{int} and Ω_{ρ^0} denote the step-off state, $\bar{x}_{\tau_{\text{int}},\Omega_{\rho^0}}$, on an intermediate QPO that approximates a local unstable manifold state, ${}_u\bar{x}_{\tau_{\text{int}},\Omega_{\rho^0}}$. Specifically, τ_{int} denotes the propagation time along a QPO from an initial invariant curve to the invariant curve on which the step-off location lies and Ω_{ρ^0} represents the modified latitudinal angle of the step-off location. The ${}_u x^{\mathbb{T}}_{\tau_{\text{int}},\Omega_{\rho^0}}$, ${}_u y^{\mathbb{T}}_{\tau_{\text{int}},\Omega_{\rho^0}}$ and ${}_u z^{\mathbb{T}}_{\tau_{\text{int}},\Omega_{\rho^0}}$ components represent the x, y and z positions of an unstable manifold state, ${}_u\bar{x}^{\mathbb{T}}_{\tau_{\text{int}},\Omega_{\rho^0}}$. The ${}_u\bar{x}^{\mathbb{T}}_{\tau_{\text{int}},\Omega_{\rho^0}}$ state is computed by propagating the ${}_u\bar{x}_{\tau_{\text{int}},\Omega_{\rho^0}}$ state for time $\mathbb{T}$. The local manifold state, ${}_u\bar{x}_{\tau_{\text{int}},\Omega_{\rho^0}}$, is approximated through the following expression,

$${}_u\bar{x}_{\tau_{\text{int}},\Omega_{\rho^0}} = \bar{x}_{\tau_{\text{int}},\Omega_{\rho^0}} + \nabla_u \frac{\boldsymbol{\Phi}_{\tau_{\text{int}},\Omega_{\rho^0}} \bar{v}_u}{\sqrt{(\boldsymbol{\Phi}_{\tau_{\text{int}},\Omega_{\rho^0}} \bar{v}_u)^T (\boldsymbol{\Phi}_{\tau_{\text{int}},\Omega_{\rho^0}} \bar{v}_u)}} \tag{32}$$

where, ∇_u signifies the step-off factor, $\bar{v}_u$ is a 6×1 unstable eigenvector associated with a state on a QPO on an initial curve at Ω_{ρ^0} angle, and $\boldsymbol{\Phi}_{\tau_{\text{int}},\Omega_{\rho^0}}$ is the STM propagated from an initial state on a QPO to $\bar{x}_{\tau_{\text{int}},\Omega_{\rho^0}}$. The step-off factor is assumed to be constant during the differential corrections process. The Jacobian matrix for eq. (56) is formulated as,

$$\mathbf{DF}(\bar{X}) = \begin{bmatrix} {}_u\dot{x}^{\mathbb{T}}_{\tau_{\text{int}},\Omega_{\rho^0}} & -\dot{x}^{\tau_{\text{arr}}}_{\text{arr}} & \frac{\partial\left({}_u x^{\mathbb{T}}_{\tau_{\text{int}},\Omega_{\rho^0}}\right)}{\partial \tau_{\text{int}}} & \frac{\partial\left({}_u x^{\mathbb{T}}_{\tau_{\text{int}},\Omega_{\rho^0}}\right)}{\partial \Omega_{\rho^0}} \\ {}_u\dot{y}^{\mathbb{T}}_{\tau_{\text{int}},\Omega_{\rho^0}} & -\dot{y}^{\tau_{\text{arr}}}_{\text{arr}} & \frac{\partial\left({}_u y^{\mathbb{T}}_{\tau_{\text{int}},\Omega_{\rho^0}}\right)}{\partial \tau_{\text{int}}} & \frac{\partial\left({}_u y^{\mathbb{T}}_{\tau_{\text{int}},\Omega_{\rho^0}}\right)}{\partial \Omega_{\rho^0}} \\ {}_u\dot{z}^{\mathbb{T}}_{\tau_{\text{int}},\Omega_{\rho^0}} & -\dot{z}^{\tau_{\text{arr}}}_{\text{arr}} & \frac{\partial\left({}_u z^{\mathbb{T}}_{\tau_{\text{int}},\Omega_{\rho^0}}\right)}{\partial \tau_{\text{int}}} & \frac{\partial\left({}_u z^{\mathbb{T}}_{\tau_{\text{int}},\Omega_{\rho^0}}\right)}{\partial \Omega_{\rho^0}} \end{bmatrix} \tag{33}$$

where, the first and second column elements are the velocity components of the propagated manifold state and the downstream arrival orbit state. The third and fourth columns comprise of the partial derivatives of the downstream manifold state with respect to the τ_{int} and Ω_{ρ^0}, respectively. These two partial derivatives are rewritten in an expanded form similar to the ones derived by McCarthy et al. [32] as,

$$\frac{\partial\left({}_u\bar{x}^{\mathbb{T}}_{\tau_{\text{int}},\Omega_{\rho^0}}\right)}{\partial \tau_{\text{int}}} = \boldsymbol{\phi}_M(\mathbb{T}, 0) \frac{\partial\left({}_u\bar{x}_{\tau_{\text{int}},\Omega_{\rho^0}}\right)}{\partial \tau_{\text{int}}} \tag{34}$$

$$\frac{\partial\left({}_u\bar{x}^{\mathbb{T}}_{\tau_{\text{int}},\Omega_{\rho^0}}\right)}{\partial \Omega_{\rho^0}} = \boldsymbol{\phi}_M(\mathbb{T}, 0) \frac{\partial\left({}_u\bar{x}_{\tau_{\text{int}},\Omega_{\rho^0}}\right)}{\partial \Omega_{\rho^0}} \tag{35}$$

The $\boldsymbol{\phi}_M(\mathbb{T},0)$ matrix is an STM that maps the first-order linear variations of the ${}_u\bar{x}_{\tau_{\text{int},\Omega_{\rho^0}}}$ state to a downstream state at time $\mathbb{T}$. The expanded form of $\frac{\partial\left({}_u\bar{x}_{\tau_{\text{int},\Omega_{\rho^0}}}\right)}{\partial\tau_{\text{int}}}$ is expressed as,

$$\begin{aligned}\frac{\partial({}_u\bar{x}_{\tau_{\text{int}},\Omega_{\rho^0}})}{\partial\tau_{\text{int}}} = \dot{\bar{x}}_{\tau_{\text{int},\Omega_{\rho^0}}} + \nabla_u\Bigg(&\frac{\dot{\boldsymbol{\Phi}}_{\tau_{\text{int}},\Omega_{\rho^0}}\bar{v}_u}{\sqrt{(\boldsymbol{\Phi}_{\tau_{\text{int}},\Omega_{\rho^0}}\bar{v}_u)^T(\boldsymbol{\Phi}_{\tau_{\text{int}},\Omega_{\rho^0}}\bar{v}_u)}}\\ &-\frac{\boldsymbol{\Phi}_{\tau_{\text{int}},\Omega_{\rho^0}}\bar{v}_u(\dot{\boldsymbol{\Phi}}_{\tau_{\text{int}},\Omega_{\rho^0}}\bar{v}_u)^T(\boldsymbol{\Phi}_{\tau_{\text{int}},\Omega_{\rho^0}}\bar{v}_u)}{2((\boldsymbol{\Phi}_{\tau_{\text{int}},\Omega_{\rho^0}}\bar{v}_u)^T(\boldsymbol{\Phi}_{\tau_{\text{int}},\Omega_{\rho^0}}\bar{v}_u))^{\frac{3}{2}}}\\ &-\frac{\boldsymbol{\Phi}_{\tau_{\text{int}},\Omega_{\rho^0}}\bar{v}_u(\boldsymbol{\Phi}_{\tau_{\text{int}},\Omega_{\rho^0}}\bar{v}_u)^T(\dot{\boldsymbol{\Phi}}_{\tau_{\text{int}},\Omega_{\rho^0}}\bar{v}_u)}{2((\boldsymbol{\Phi}_{\tau_{\text{int}},\Omega_{\rho^0}}\bar{v}_u)^T(\boldsymbol{\Phi}_{\tau_{\text{int}},\Omega_{\rho^0}}\bar{v}_u))^{\frac{3}{2}}}\Bigg)\end{aligned} \tag{36}$$

where, $\dot{\boldsymbol{\Phi}}_{\tau_{\text{int}},\Omega_{\rho^0}}$ is the time derivative of matrix $\boldsymbol{\Phi}_{\tau_{\text{int}},\Omega_{\rho^0}}$. The partial derivative $\frac{\partial\left({}_u\bar{x}_{\tau_{\text{int},\Omega_{\rho^0}}}\right)}{\partial\Omega_{\rho^0}}$ is written as,

$$\frac{\partial\left({}_u\bar{x}_{\tau_{\text{int},\Omega_{\rho^0}}}\right)}{\partial\Omega_{\rho^0}} = \frac{\partial\left(\bar{x}_{\tau_{\text{int},\Omega_{\rho^0}}}\right)}{\partial\Omega_{\rho^0}} + \nabla_u\frac{\partial\left(\boldsymbol{\Phi}_{\tau_{\text{int}},\Omega_{\rho^0}}\bar{v}_u\left(\sqrt{(\boldsymbol{\Phi}_{\tau_{\text{int}},\Omega_{\rho^0}}\bar{v}_u)^T(\boldsymbol{\Phi}_{\tau_{\text{int}},\Omega_{\rho^0}}\bar{v}_u)}\right)^{-1}\right)}{\partial\Omega_{\rho^0}} \tag{37}$$

It is evident that the above partial derivative requires the computation of $\frac{\partial\left(\boldsymbol{\Phi}_{\tau_{\text{int}},\Omega_{\rho^0}}\right)}{\partial\Omega_{\rho^0}}$ term, which is challenging due to the lack of an analytical expression as noted by McCarthy et al. [32]. A different method than the ones formulated by McCarthy et al. [8, 32] is adopted to evaluate eq. (37) that relies on the construction of an unstable eigenvector spectrum of the invariant curve on which $\bar{x}_{\tau_{\text{int},\Omega_{\rho^0}}}$ state lies. The partial derivative, eq. (37), is rewritten as,

$$\frac{\partial\left({}_u\bar{x}_{\tau_{\text{int},\Omega_{\rho^0}}}\right)}{\partial\Omega_{\rho^0}} = \frac{\partial\left(\bar{x}_{\tau_{\text{int},\Omega_{\rho^0}}}\right)}{\partial\Omega_{\rho^0}} + \nabla_u\frac{\partial\left(\bar{w}_u\left(\sqrt{\bar{w}_u^T\bar{w}_u}\right)^{-1}\right)}{\partial\Omega_{\rho^0}} \tag{38}$$

$$= \frac{\partial\left(\bar{x}_{\tau_{\text{int},\Omega_{\rho^0}}}\right)}{\partial\Omega_{\rho^0}} + \nabla_u\Bigg(\frac{\frac{\partial\bar{w}_u}{\partial\Omega_{\rho^0}}}{\sqrt{\bar{w}_u^T\bar{w}_u}} - \frac{\bar{w}_u\left(\left(\frac{\partial\bar{w}_u}{\partial\Omega_{\rho^0}}\right)^T\bar{w}_u + \bar{w}_u^T\frac{\partial\bar{w}_u}{\partial\Omega_{\rho^0}}\right)}{2(\bar{w}_u^T\bar{w}_u)^{\frac{3}{2}}}\Bigg) \tag{39}$$

where, $\bar{w}_u = \boldsymbol{\Phi}_{\tau_{\text{int},\Omega_{\rho^0}}}\bar{v}_u$ is an unstable eigenvector corresponding to the step-off state, $\bar{x}_{\tau_{\text{int},\Omega_{\rho^0}}}$. The derivative of the step-off state with respect to Ω_{ρ^0} is given as,

$$\frac{\partial\left(\bar{x}_{\tau_{\text{int},\Omega_{\rho^0}}}\right)}{\partial\Omega_{\rho^0}} = \text{diag}[\text{i}\bar{k}]\text{e}^{\text{i}\bar{k}\Omega_{\rho^0}}\mathbf{C}_0 \tag{40}$$

Recall, $\bar{k}$ is defined in eq. (24), and $\mathbf{C}_0$ matrix comprises the Fourier coefficients corresponding to the states that describe the initial invariant curve on the QPO, similar to eq. (21). The partial derivative of the unstable eigenvector with respect to the modified latitudinal angle in eq. (39) is evaluated using the Fourier coefficients of the unstable eigenvector spectrum associated with the invariant curve of the intermediate QPO that comprises of $\bar{x}_{\tau_{\text{int},\Omega_{\rho^0}}}$ state,

$$\frac{\partial\bar{w}_u}{\partial\Omega_{\rho^0}} = \text{diag}[\text{i}\bar{k}]\text{e}^{\text{i}\bar{k}\Omega_{\rho^0}}\mathbf{C}_u \tag{41}$$

The $\mathbf{C}_u$ matrix consists of the Fourier coefficients of the unstable eigenvector spectrum and is computed through the following,

$$\mathbf{C}_u = \mathbf{D}\mathbf{W}_u \tag{42}$$

where, $\mathbf{D}$ denotes the discrete Fourier transform operator as defined in eq. (23), and $\mathbf{V}_u$ matrix comprises of the unstable eigenvectors of the states that approximate the invariant curve, which is τ_{int} downstream from the initial invariant curve, and it is structured similar to eq. (20). The downstream eigenvector spectrum is computed through the block diagonal STM, $\tilde{\mathbf{\Phi}}(\tau_{\text{int}}, 0)$, which is similar to the one mentioned in eq. (27), and unstable eigenvector spectrum of the initial invariant curve, $\mathbf{V}_u$, through the following expression,

$$\mathbf{W}_u = \tilde{\mathbf{\Phi}}(\tau_{\text{int}}, 0)\mathbf{V}_u \tag{43}$$

It is evident that the shooting method formulation in eq. (56) is underconstrained, hence, the solutions are determined through the minimum-norm update formulation of the Newton-Raphson method.

For an intermediate QPO, the differential corrections scheme for construction of an inbound segment, eq. (33), comprises *1-dimensional* null-space. Hence, the solutions exist as a *1-parameter* family and are generated through the pseudo-arc length continuation scheme. This scheme is employed for the construction of local families of solutions with the initial guess identified in fig. 12 through the selected L_2 quasi-vertical orbit. Two distinct families of solutions in region 1, as highlighted in fig. 16, and its mirror configuration about the $\hat{x} - \hat{y}$ plane are constructed and represented in fig. 20. The solutions obtained through the initial guess in region 2, marked in fig. 16, are not plotted in fig. 20 as they lead to higher maneuver cost solutions with multiple options that traverse through the surface of the Moon. A few members of the families marked by 1' and 2 as depicted in fig. 20 are visualized in the configuration space in fig. 21. The outlined initial guess generation methodology is utilized to select an L_2 quasi-P2HO$_2$ orbit with $\rho^0 = 1.59184$ rad, plotted in fig. 13 as the representative member of its constant energy family. The initial guess derived from the selected L_2quasi-P2HO$_2$ orbit is employed to uncover the solutions depicted in fig. 22. The *1-parameter* family of segments generated through intermediate QPOs afford transfer options to mission designers to select the pathways that meet any desired operational constraints.

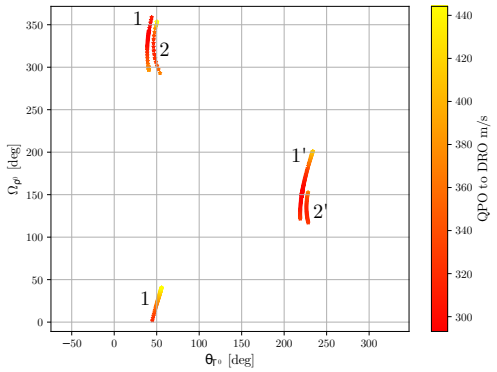

Fig. 20 Differential corrected inbound segments to the arrival orbit constructed through the initial guess obtained in fig. 16. The solutions in the local basins 1' and 2' are mirror configurations of the options in local basins 1 and 2 about the $\hat{x} - \hat{y}$ plane.

For intermediate periodic orbits, a similar differential corrections procedure as that for an intermediate QPO is developed with the difference that a single parameter is required to describe the step-off location of a manifold arc. The design and constraint vector for the scheme are formulated as,

$$\bar{X} = \begin{bmatrix} \mathbb{T} \\ \tau_{\text{arr}} \\ \tau_{\text{int}} \end{bmatrix}; \quad \bar{F}(\bar{X}) = \begin{bmatrix} u x^{\mathbb{T}}_{\tau_{\text{int}}} - x^{\tau_{\text{arr}}}_{\text{arr}} \\ u y^{\mathbb{T}}_{\tau_{\text{int}}} - y^{\tau_{\text{arr}}}_{\text{arr}} \\ u z^{\mathbb{T}}_{\tau_{\text{int}}} - z^{\tau_{\text{arr}}}_{\text{arr}} \end{bmatrix} \tag{44}$$

where, $\mathbb{T}$, τ_{arr}, and $(x^{\tau_{\text{arr}}}_{\text{arr}}, y^{\tau_{\text{arr}}}_{\text{arr}}, z^{\tau_{\text{arr}}}_{\text{arr}})$ represent the quantities as previously defined for the intermediate QPO case. The τ_{int} captures the step-off location of a manifold arc in terms of the propagating time from an initial state along the

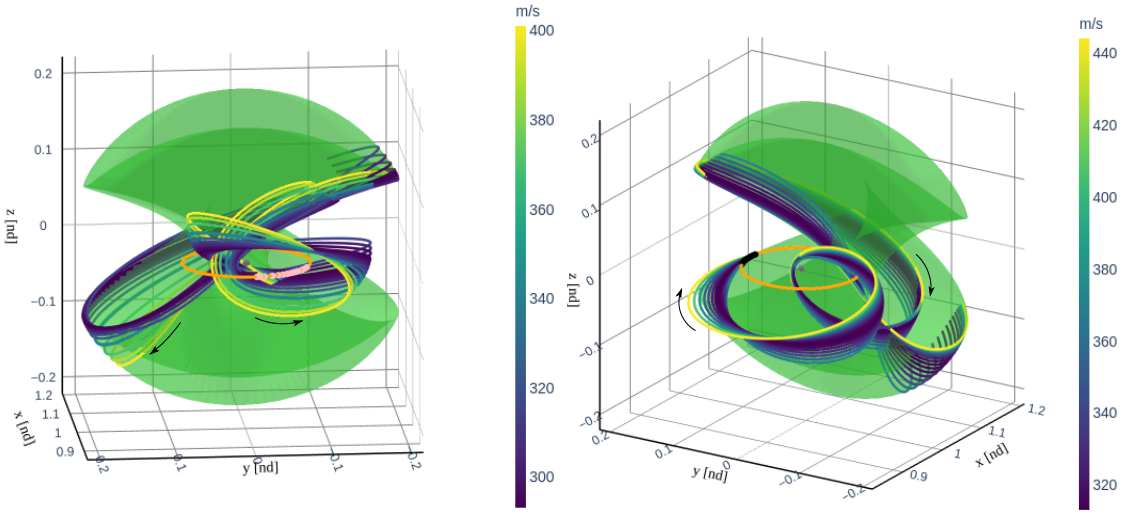

(a) Solutions of the local basin 1'. **(b) Solutions of the local basin 2**

Fig. 21 Transfer geometries corresponding to the local basin 1' and 2 as highlighted in fig. 20. The local solutions generated with an L_2 quasi-vertical orbit (green) as the intermediate orbit require a single maneuver (pink/black in the left/right plot) to overcome the velocity discontinuity with the arrival orbit (orange). The time of flight of the segments ranges from 26.8 to 28.1 days.

intermediate periodic orbit. The ${}_u\bar{x}^{\mathbb{T}}_{\tau_{\text{int}}}$ state is an unstable manifold state that is computed by propagating a local manifold state corresponding to the $\bar{x}_{\tau_{\text{int}}}$ step-off location for time $\mathbb{T}$. The local manifold state, ${}_u\bar{x}_{\tau_{\text{int}}}$, is approximated through the following expression,

$$ {}_u\bar{x}_{\tau_{\text{int}}} = \bar{x}_{\tau_{\text{int}}} + \nabla_u \frac{\boldsymbol{\Phi}_{\tau_{\text{int}}} \bar{v}_u}{\sqrt{(\boldsymbol{\Phi}_{\tau_{\text{int}}} \bar{v}_u)^T (\boldsymbol{\Phi}_{\tau_{\text{int}}} \bar{v}_u)}} \tag{45} $$

where, ∇_u represents a step-off factor (dimensionless), $\bar{v}_u$ corresponds to a 6×1 unstable eigenvector associated with the initial state of an intermediate orbit, and $\boldsymbol{\Phi}_{\tau_{\text{int}}}$ is the STM that maps the first-order effect of variations in the initial state of an orbit to $\bar{x}_{\tau_{\text{int}}}$ state. The manifold step-off factor is assumed to be constant during the differential corrections process. The Jacobian matrix of the differential corrections scheme is given by,

$$ \mathbf{DF}(\bar{X}) = \begin{bmatrix} {}_u\dot{x}^{\mathbb{T}}_{\tau_{\text{int}}} & -\dot{x}^{\tau_{\text{arr}}}_{\text{arr}} & \frac{\partial({}_u x^{\mathbb{T}}_{\tau_{\text{int}}})}{\partial \tau_{\text{int}}} \\ {}_u\dot{y}^{\mathbb{T}}_{\tau_{\text{int}}} & -\dot{y}^{\tau_{\text{arr}}}_{\text{arr}} & \frac{\partial({}_u y^{\mathbb{T}}_{\tau_{\text{int}}})}{\partial \tau_{\text{int}}} \\ {}_u\dot{z}^{\mathbb{T}}_{\tau_{\text{int}}} & -\dot{z}^{\tau_{\text{arr}}}_{\text{arr}} & \frac{\partial({}_u z^{\mathbb{T}}_{\tau_{\text{int}}})}{\partial \tau_{\text{int}}} \end{bmatrix} \tag{46} $$

The first and the second column of the Jacobian matrix are the velocity components of ${}_u\bar{x}^{\mathbb{T}}_{\tau_{\text{int}}}$ and $\bar{x}^{\tau_{\text{arr}}}_{\text{arr}}$, respectively. The elements in the third column correspond to the variation in the position of the downstream manifold state with respect to the change in the step-off location on the intermediate periodic orbit. The partial derivative of the change in downstream manifold state with respect to τ_{int} is expressed as,

$$ \frac{\partial({}_u\bar{x}^{\mathbb{T}}_{\tau_{\text{int}}})}{\partial \tau_{\text{int}}} = \boldsymbol{\phi}_M(\mathbb{T}, 0) \frac{\partial({}_u\bar{x}_{\tau_{\text{int}}})}{\partial \tau_{\text{int}}} \tag{47} $$

where, $\boldsymbol{\phi}_M(\mathbb{T}, 0)$ is an STM that captures the impact of change in ${}_u\bar{x}_{\tau_{\text{int}}}$ state on the ${}_u\bar{x}^{\mathbb{T}}_{\tau_{\text{int}}}$ state. The derivative of ${}_u\bar{x}_{\tau_{\text{int}}}$ with respect to τ_{int} is written as,

$$ \frac{\partial({}_u\bar{x}_{\tau_{\text{int}}})}{\partial \tau_{\text{int}}} = \dot{\bar{x}}_{\tau_{\text{int}}} + \nabla_u \left(\frac{\dot{\boldsymbol{\Phi}}_{\tau_{\text{int}}} \bar{v}_u}{\sqrt{(\boldsymbol{\Phi}_{\tau_{\text{int}}} \bar{v}_u)^T (\boldsymbol{\Phi}_{\tau_{\text{int}}} \bar{v}_u)}} - \frac{\boldsymbol{\Phi}_{\tau_{\text{int}}} \bar{v}_u ((\dot{\boldsymbol{\Phi}}_{\tau_{\text{int}}} \bar{v}_u)^T (\boldsymbol{\Phi}_{\tau_{\text{int}}} \bar{v}_u) + (\boldsymbol{\Phi}_{\tau_{\text{int}}} \bar{v}_u)^T (\dot{\boldsymbol{\Phi}}_{\tau_{\text{int}}} \bar{v}_u))}{2((\boldsymbol{\Phi}_{\tau_{\text{int}}} \bar{v}_u)^T (\boldsymbol{\Phi}_{\tau_{\text{int}}} \bar{v}_u))^{\frac{3}{2}}} \right) \tag{48} $$

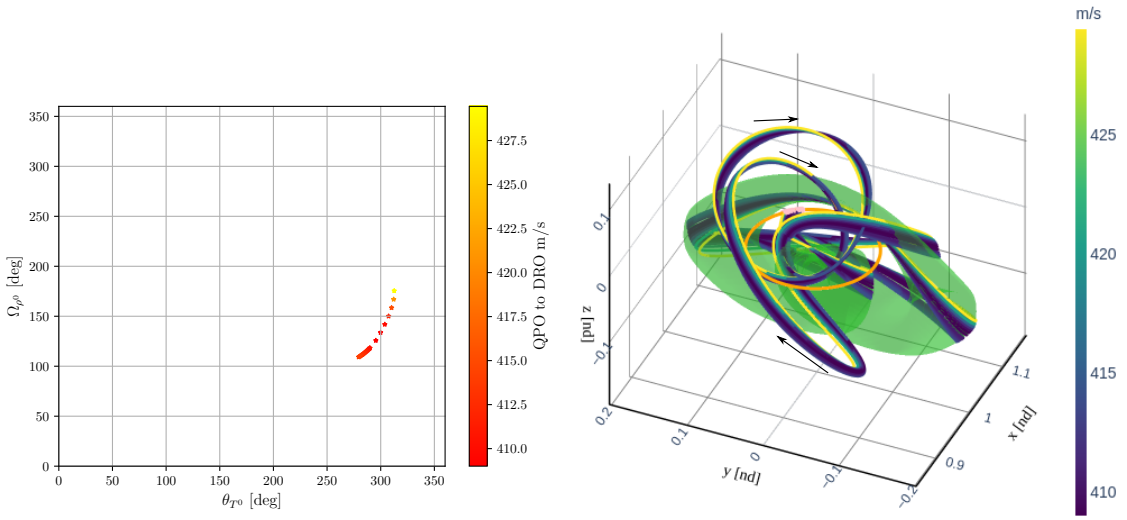

(a) Heat map representation **(b) Configuration space plot**

Fig. 22 Inbound segments obtained through the unstable manifold associated with an L_2 quasi-P2HO$_2$ orbit (green) plotted on a heat map and configuration space. The time of flight of the segments ranges from 46.8 days to 47.2 days.

where, $\dot{\mathbf{\Phi}}_{\tau_{\text{int}}}$ is the time derivative of matrix $\mathbf{\Phi}_{\tau_{\text{int}}}$. The partial derivatives in the third column of the Jacobian matrix, eq. (46), are the first three components of eq. (47). The shooting method, eq. (44), is fully constrained, hence, the initial guess from a manifold arc of an intermediate periodic orbit leads to a locally unique solution. The initial guess obtained from the L_2 vertical orbit in fig. 14 are fed to the corrections scheme and the resultant solutions are plotted in fig. 23(a). Similarly, the initial guess is generated for L_2 P2HO$_2$ orbit, 3:4 RPO and DPO and their converged segments are visualized in figs. 23(b), 24(a) and 24(b), respectively. The transfer maneuver costs and flight times for the segments generated through the four selected intermediate orbits are tabulated in tables 3 to 6. Recall that the RPO and DPO are only employed as the second intermediate orbit for the design of the exterior-type transfrs. It is notable that the transfer geometries realized through L_2 vertical and L_2 P2HO$_2$ orbits are more fuel-expensive than the solutions obtained from their QPO counterparts. Additionally, the two intermediate QPOs offer many more options than their underlying periodic orbits.

B. Outbound Segment from the Departure Orbit

The design of the outbound segment from the departure orbit to an intermediate orbit follows a similar approach to the inbound segment. However, it incorporates stable manifold arcs associated with the intermediate orbit, in contrast to the unstable manifold arcs employed in the inbound segment. Additionally, the solutions are position continuous with the departure orbit, rather than the arrival orbit, as in the case of the inbound segment. A continuous representation of the NRHO is generated in the same manner as that for the DRO to formulate an events function to identify potential candidates of the stable manifold arcs. The differential corrections schemes described for the the inbound segment are leveraged with the noted difference of the use of stable manifold arcs and departure orbit. Consistent with the inbound segments, solutions derived from intermediate periodic orbits are locally unique and those constructed through intermediate QPOs appear as *1-parameter* family of solutions. The inherent difference in the solution space offered by the two types of orbit is linked to the dimensionality of their stable manifolds.

The single maneuver outbound segments realized from the selected intermediate periodic and quasi-periodic orbits are plotted in the configuration space and their associated maneuver costs are tabulated. The solutions derived from the L_2 vertical and L_2 P2HO$_2$ orbits are depicted in fig. 25, and their associated costs are provided in tables 7 and 8. Each of the two intermediate periodic orbits gives rise to two locally unique outbound segments. The two previously selected intermediate QPOs, L_2 quasi-vertical (rad=0.42259 rad) and L_2 quasi-P2HO$_2$ (rad=1.59184 rad), uncover multiple *1-parameter* families of segments as represented in figs. 26 and 27. It is of note that only the low maneuver cost solutions that maintain a perilune distance greater than the radius of the Moon are considered. It is evident from the

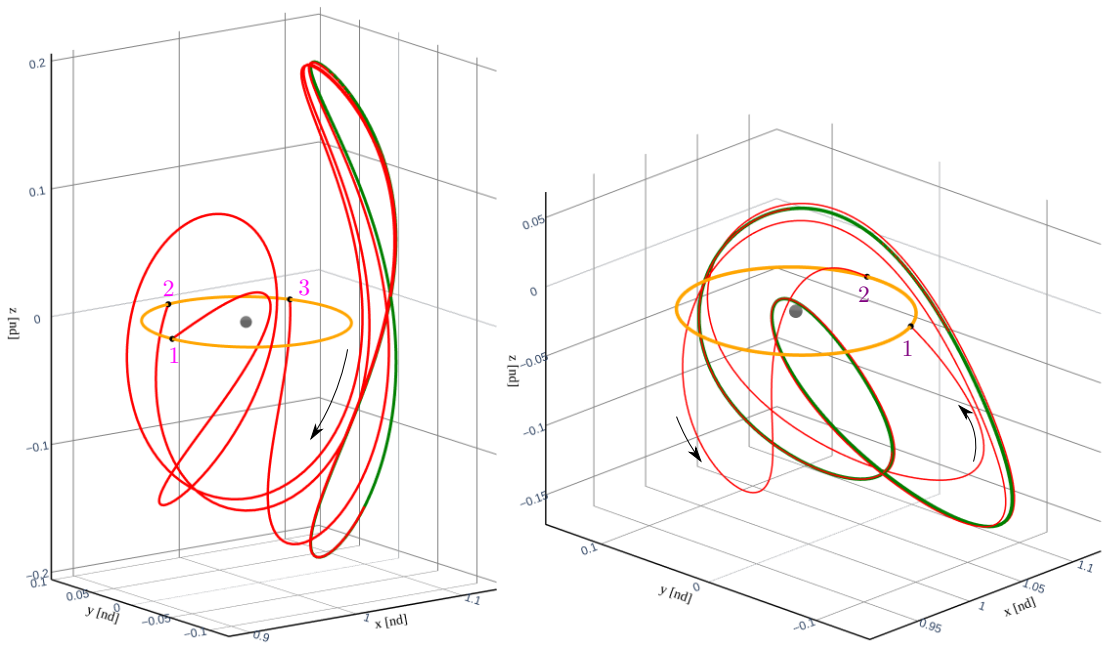

(a) Derived from the L_2 vertical orbit **(b) Derived from the L_2 P2HO$_2$ orbit**

Fig. 23 Three and two converged inbound segments informed by an L_2 vertical and L_2 P2HO$_2$, respectively. The segments require a single impulsive maneuver (black) to overcome the velocity discontinuity with the DRO. The maneuver costs and flight times for the L_2 vertical and L_2 P2HO$_2$ are tabulated in table 3 and table 4, respectively.

visuals that the two intermediate QPOs offer more solutions with lower maneuver-costs compared to ones generated from their underlying periodic orbits.

C. Interior-type Transfers

The interior-type pathways, with reasonable maneuver cost and flight times, between the departure and arrival orbit are designed by stitching an outbound segment from the departure orbit, a bridging arc, and an inbound segment to the arrival orbit. The construction of the outbound and inbound segments are informed by the stable and unstable manifolds associated with a selected intermediate orbit as elucidated in sections III.A and III.B, respectively. The two segments are linked by a bridging arc that is generated by leveraging the natural flow of the intermediate orbit. Thereafter, the three segments are differentially corrected for full-state continuity such that the resultant geometry only requires a departure and an arrival maneuver to connect the two orbits as illustrated in fig. 9. The differential corrections scheme is defined to vary the time of flight of the segments, as well as the departure and arrival locations. Subsequently, the corrected solution is seeded as an initial guess to a multiple shooting transcribed optimization scheme to identify locally fuel-optimal transfers.

Due to the repeatable geometry of a periodic orbit, it is feasible to link any pair of outbound and inbound segments that are derived from an intermediate periodic orbit to design interior-type transfers. The design of a bridging arc is initiated by flowing the outbound segment from the departure orbit forward in time for a time period ascertained by the difference in the step-off location of the local manifold states corresponding to the outbound and inbound segments. The step-off location of the stable and unstable manifold states that serve as the initial state for their respective segments are represented in terms of the propagation time from an initial state along the orbit and expressed as $\tau_{\text{int,dep}}$ and $\tau_{\text{int,arr}}$, respectively. The estimate for the flight of time of the bridging arc is evaluated as,

$$\mathfrak{T}_{\text{PO}} = \text{mod}(\mathbb{P}_{\text{int}} + \tau_{\text{int,arr}} - \tau_{\text{int,dep}}, \quad \mathbb{P}_{\text{int}}) \tag{49}$$

where, where, $\mathfrak{T}_{\text{PO}}$ denotes the approximate flight time of the bridging arc and $\mathbb{P}_{\text{int}}$ represents the period of the intermediate periodic orbit. The modulo operator, mod, ensures that the bridging arc flight time does not exceed the

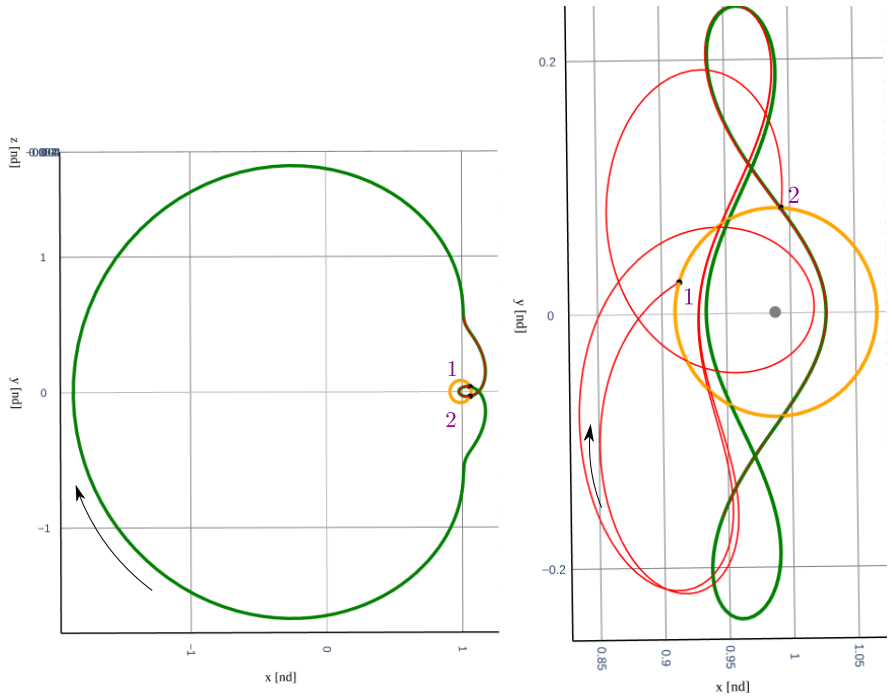

(a) Derived from the 3:4 RPO (b) Derived from the DPO

Fig. 24 Two converged inbound segments informed by an 3:4 RPO and a DPO, respectively. The segments require a single impulsive maneuver (black) to overcome the velocity discontinuity with the DRO. The maneuver costs and flight times for the RPO and DPO are tabulated in table 5 and table 6, respectively.

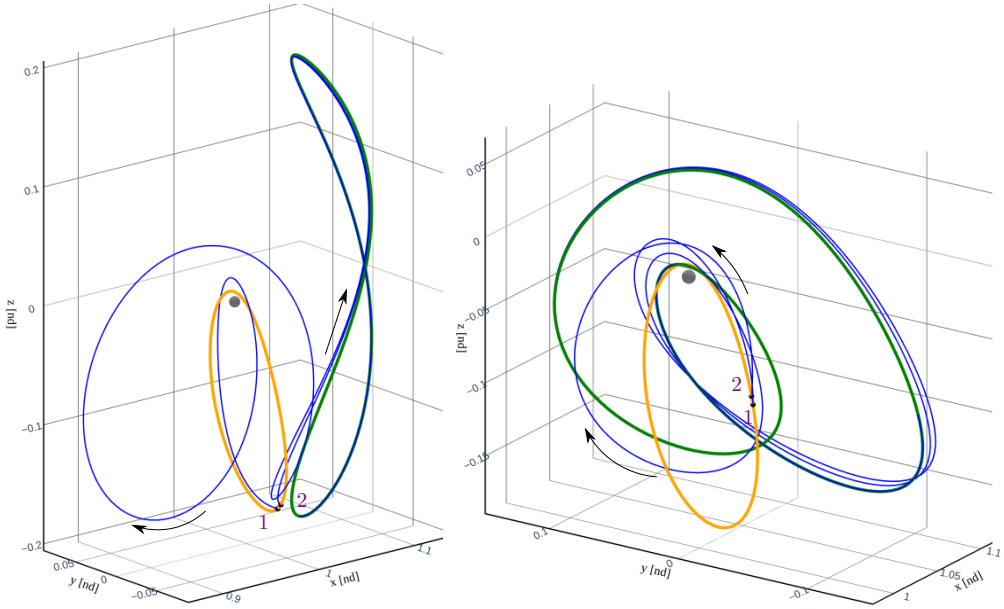

(a) Derived from the L_2 vertical orbit (b) Derived from the L_2 P2HO$_2$ orbit

Fig. 25 Two converged outbound segments informed by an L_2 vertical and L_2 P2HO$_2$, respectively. The segments require a single impulsive maneuver (black) to overcome the velocity discontinuity with the DRO. The maneuver costs and flight times for the L_2 vertical and L_2 P2HO$_2$ are tabulated in table 7 and table 8, respectively.

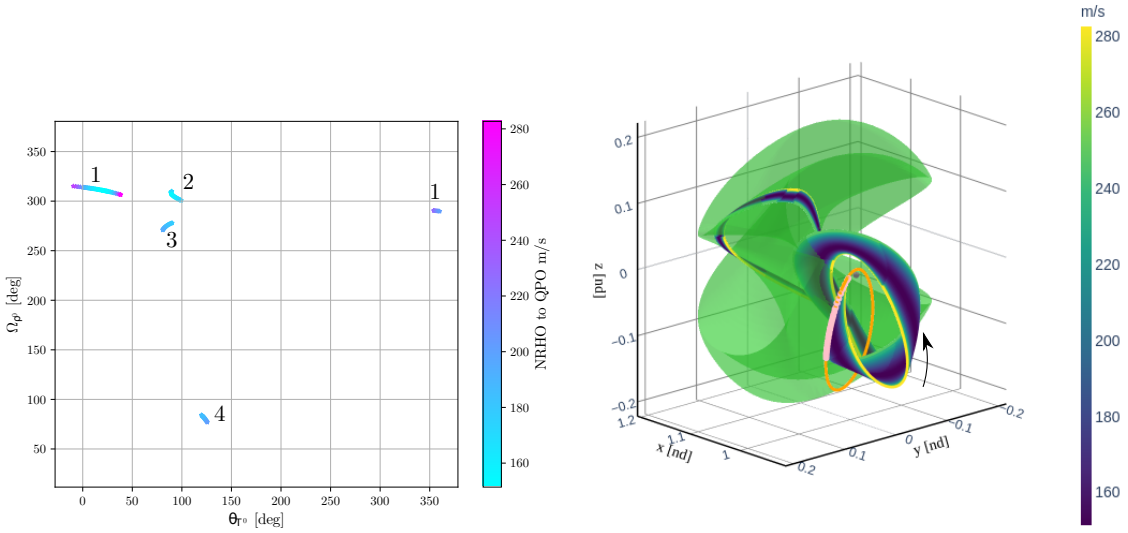

(a) Heat map representation **(b) Configuration space plot of family 1**

Fig. 26 Outbound segments obtained through the stable manifold arcs associated with an L_2 quasi-vertical orbit (green) plotted on a heat map and family 1 is plotted in the configuration space. The departure maneuver locations in the configuration space are marked by the pink dots. The time of flight of the segments ranges from 26.8 to 28.1 days.

period of the intermediate orbit. It is apparent from the formulation that the bridging arc is full-state continuous with the outbound segment but discontinuous with the inbound segment. Hence, the aforementioned differential corrections scheme is employed to link the three segments to construct a two-maneuver transfer that connects the two orbits. The lowest maneuver cost outbound and inbound segments designed via the L_2 vertical orbit and L_2 P2HO$_2$ orbit, as tabulated in tables 3, 4, 7 and 8, are selected to realize the interior-type transfers depicted in fig. 28.

The design of the bridging arc to link the outbound and inbound segments constructed through the stable and unstable manifolds associated with an intermediate QPO is complicated due to the non-repeatable nature of QPO. For the construction of low maneuver cost and short TOF solutions, the choice of outbound and inbound segments is narrowed down to segments with step-off locations that lie in the immediate upstream or downstream of each other. Consider the step-off location on the QPO associated with the local manifold state corresponding to the outbound and inbound segment be represented as $\bar{x}_{\text{int,dep}}$ and $\bar{x}_{\text{int,arr}}$, respectively. The $\bar{x}_{\text{int,dep}}$ and $\bar{x}_{\text{int,arr}}$ states are alternatively expressed as $(\theta_{T^0,\text{dep}},\ \Omega_{\rho^0,\text{dep}})$ and $(\theta_{T^0,\text{arr}},\ \Omega_{\rho^0,\text{arr}})$. To identify the segments that meet the desired criteria, the following expression is employed,

$$\Omega_{\rho^0,\text{arr}} \approx \text{mod}(\Omega_{\rho^0,\text{dep}} + \text{n}_{\text{rev}}\rho^0,\quad 2\pi) \tag{50}$$

where, n_{rev} is an integer number that represents the number of revolutions around a QPO that an $\bar{x}_{\text{int,dep}}$ state is propagated to attain the desirable $\Omega_{\rho^0,\text{arr}}$ value. The selection of $\bar{x}_{\text{int,dep}}$ and $\bar{x}_{\text{int,arr}}$ states is biased to satisfy the eq. (50) with a small value of n_{rev} to uncover a bridging arc with a short TOF. For an identified value of n_{rev}, the TOF of the bridging arc is estimated as,

$$\tau_{\text{QPO}} = \frac{T^0}{2\pi}(\theta_{T^0,\text{arr}} - \theta_{T^0,\text{dep}}) + \text{n}_{\text{rev}}T^0 \tag{51}$$

where, τ_{QPO} denotes the TOF of the bridging arc. For an L_2 quasi-vertical orbit, the outbound and inbound segments as represented on a heatmap in figs. 20 and 26 are overlaid on a common plot, as presented in fig. 29(a), to identify potential candidates for the identification of suitable segment pairings. A pair of $\bar{x}_{\text{int,dep}}$ and $\bar{x}_{\text{int,arr}}$ are selected for the quasi-vertical orbit that satisfies eq. (50) for a value of n_{rev}=1 as illustrated in fig. 29(a). The stable manifold arc associated with the selected $\bar{x}_{\text{int,dep}}$ is propagated forward for τ_{QPO} evaluated through eq. (51) to get an initial guess for the briding arc. The three selected segments are connected through the described differential corrections scheme to

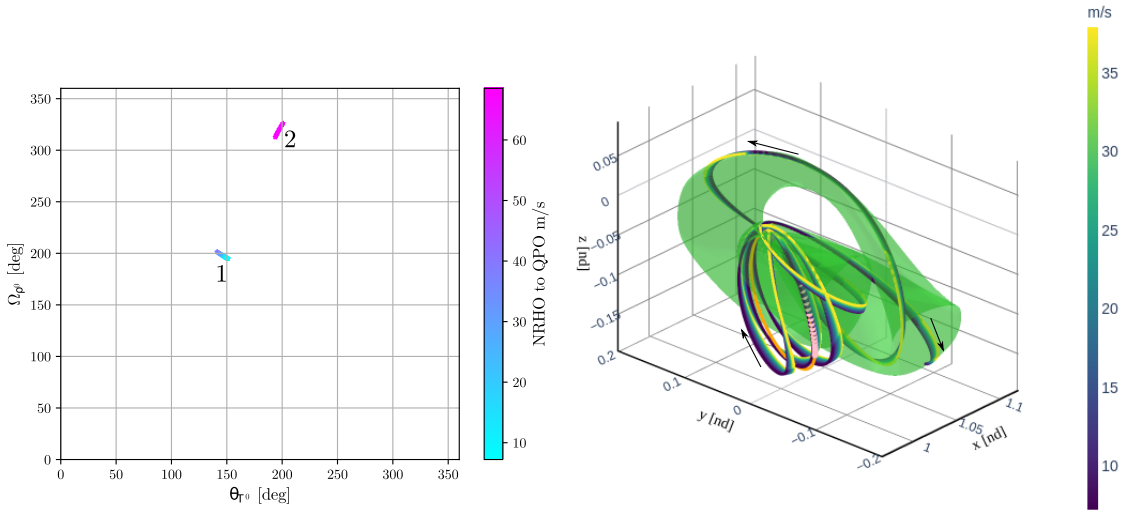

(a) Heat map representation **(b) Configuration space plot of family 1**

Fig. 27 Outbound segments obtained through the stable manifold arcs associated with an L_2 quasi-P2HO$_2$ orbit (green) plotted on a heat map and family 1 is plotted in the configuration space. The departure maneuver locations in the configuration space are marked by the pink dots. The time of flight of the segments ranges from 44.3 to 46.03 days.

reveal the interior-type transfer visualized in fig. 31(a). A similar strategy is leveraged to design a transfer through an L_2 quasi-P2HO$_2$ orbit. The heat map representation of the outbound and inbound segments are overlaid in fig. 29(b), and it is evident that the identified $\bar{x}_{\text{int,arr}}$ state does not lie in the immediate downstream, rather in the immediate upstream of the $\bar{x}_{\text{int,dep}}$ state. The specified outbound and inbound segments are plotted in the configuration space in fig. 30, and it is apparent that the two segments follow a common pathway as they approach and depart the orbit. Hence, it is feasible to connect the segments by modifying the flight time of the two segments such that the end states of the two segments lie in their vicinity. This strategy does not explicitly require a bridging arc to connect the two altered segments, and the differentially corrected geometry appears in fig. 31(b). The members of other *1-parameter* families of segments may be linked to result in alternate differentially corrected geometries derived from the manifold associated with an intermediate QPO. In general, the inbound and outbound segments, as well as the two-maneuver transfers derived from the selected intermediate QPOs, result in a greater number and lower maneuver cost solutions than their counterparts constructed from their underlying periodic orbits.

An optimization scheme is employed to uncover the locally fuel-optimal solutions that leverage the differentially corrected solutions as the initial guess. An interior point method, IPOPT [33], is utilized as the optimization technique with an objective function that minimizes $\Delta V_{\text{dep}}^2 + \Delta V_{\text{arr}}^2$. The optimization scheme is a multiple shooting transcription of the differential corrections strategy described to link the three segments. Hence, the time of flight, as well as the departure and arrival locations are allowed to vary during the optimization process. The locally fuel-optimal two maneuver interior-type transfers for the differentially corrected solutions generated through an L_2 P2HO$_2$ and an L_2 quasi-vertical orbit as visualized in figs. 28(b) and 31(a) appear in figs. 32(a) and 32(b). The presented systematic framework assists in realizing the multiple local solution basins that are fundamentally characterized by the selected intermediate orbits.

D. Exterior-type Transfers

The exterior-type transfers link the departure orbit to the arrival orbit through a pathway that traverses through the far side of the Earth. The design of this type of transfer is informed by the stable and unstable manifolds associated with two intermediate orbits as depicted in fig. 10. The construction of the transfer is decomposed into the generation of six segments: an outbound segment from the departure orbit to the first intermediate orbit, a bridging arc along the first intermediate orbit, a segment from the first intermediate orbit to the far side of the Earth (IO1Earth), a segment from the far side of the Earth to a second intermediate orbit (EarthIO2), a bridging arc along the second intermediate orbit, and

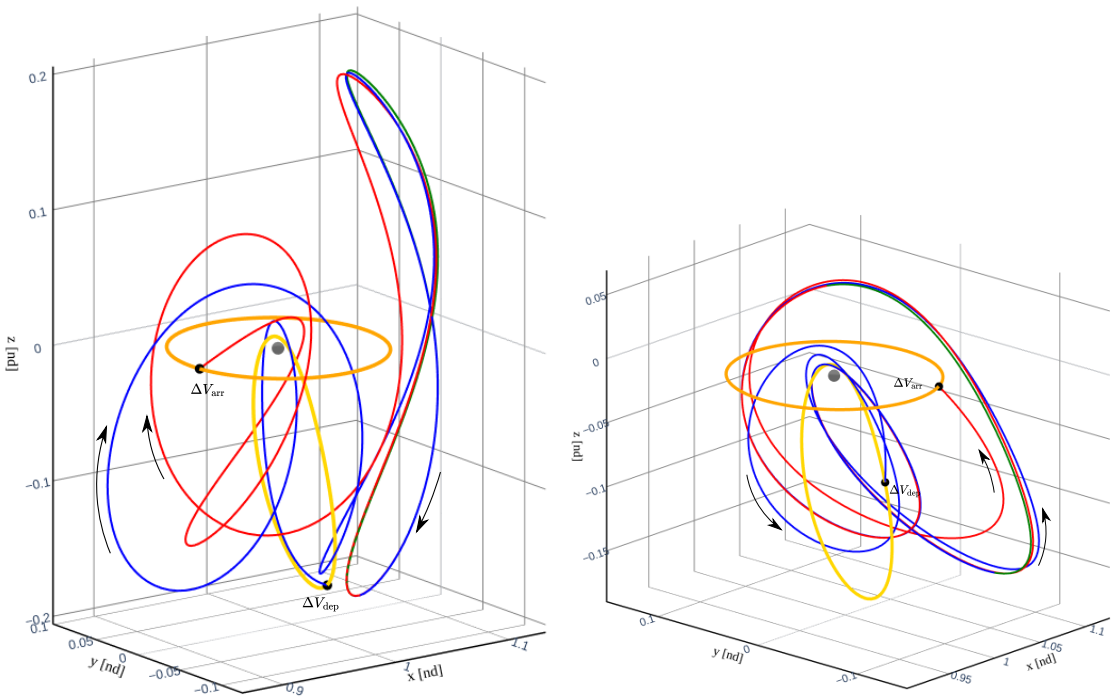

(a) Informed by an L_2 vertical orbit, $\Delta V_{tot} = \Delta V_{dep} + \Delta V_{arr}$ = 197.810 + 535.494 = 733.304 m/s, TOF = 75.745 days

(b) Informed by an L_2 P2HO$_2$ orbit, $\Delta V_{tot} = \Delta V_{dep} + \Delta V_{arr}$ = 103.387 + 602.444 = 708.831 m/s, TOF = 64.946 days

Fig. 28 Interior-type transfers informed by intermediate periodic orbits. The blue, green, and red colored portions of the full-state continuous trajectory are post differential correction remnants of the initial guess of the three segments.

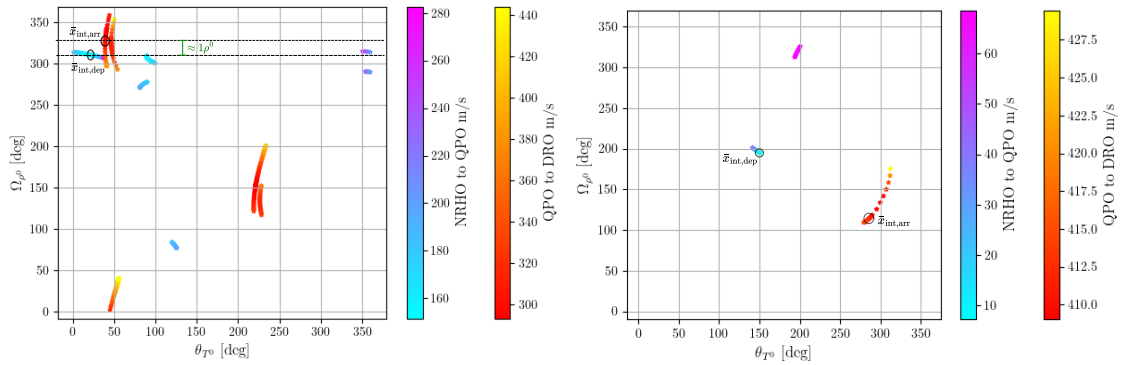

(a) L_2 quasi-vertical orbit, ρ^0 = 0.42259 rad.

(b) L_2 quasi-P2HO$_2$ orbit, ρ^0 = 1.59184 rad.

Fig. 29 Angular variable representation of stable and unstable manifold step-off locations corresponding to families of differentially corrected outbound and inbound segments constructed through an L_2 quasi-vertical orbit and an L_2 quasi-P2HO$_2$ orbit.

an inbound segment to the arrival orbit from the second intermediate orbit. The design of the outbound and inbound segments follows the same procedure as outlined in sections III.A and III.B. Additionally, the IO1Earth and EarthIO2 segments are constructed via the stable and unstable manifolds associated with the intermediate orbits. The bridging arcs are designed by leveraging the natural flow along the intermediate orbit. After the identification of the options for the six segments, they are connected via a differential corrections scheme to obtain three maneuver transfers, and the

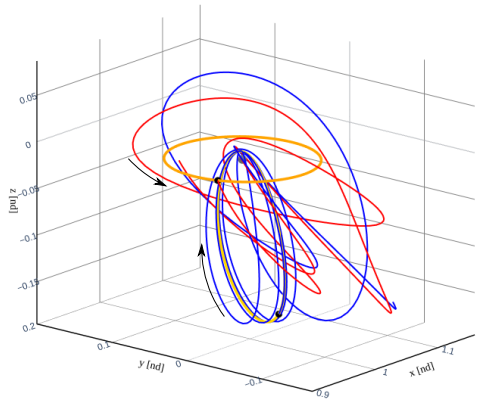

Fig. 30 Plot of an outbound and inbound segment corresponding to the selected $\bar{x}_{\text{int,dep}}$ and $\bar{x}_{\text{int,dep}}$ states in fig. 29(b).

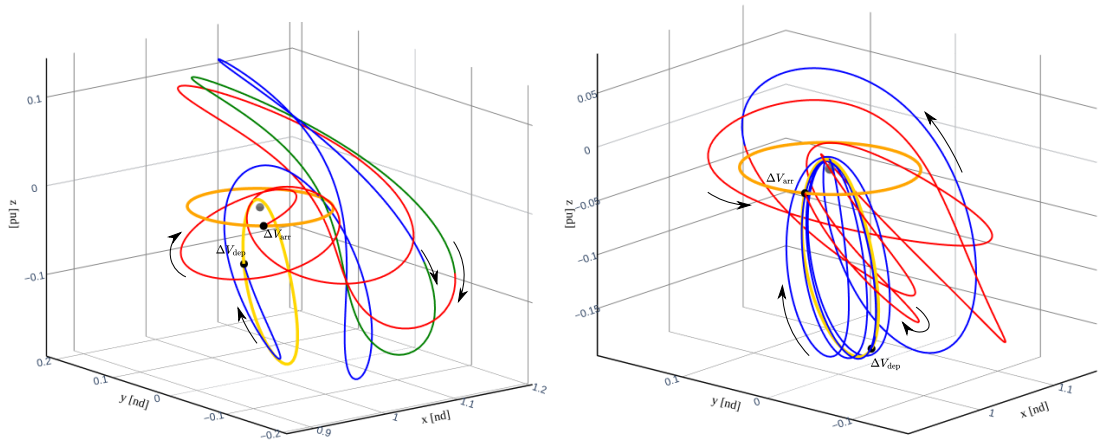

(a) Informed by an L_2 quasi-vertical orbit, $\Delta V_{\text{tot}} = \Delta V_{\text{dep}} + \Delta V_{\text{arr}}$ = 153.213 + 292.010 = 445.223 m/s, TOF = 69.938 days.

(b) Informed by an L_2 quasi-P2HO$_2$ orbit, $\Delta V_{\text{tot}} = \Delta V_{\text{dep}} + \Delta V_{\text{arr}}$ = 7.815 + 473.403 = 481.217 m/s, TOF = 73.944 days

Fig. 31 Interior-type transfers informed by intermediate quasi-periodic orbits. The blue, green, and red colored portions of the full-state continuous trajectory are post-differential correction remnants of the initial guess of the three segments.

corrections procedure is transcribed into an optimization scheme to construct locally fuel-optimal solutions.

The IO1Earth and EarthIO2 segments are identified through the unstable and stable manifold arcs associated with the first and second intermediate orbits, respectively, that reach the far side of the Earth. For an intermediate QPO, a subset of its associated *3-dimensional* unstable/stable manifold is employed for the IO1Earth/EarthIO2 segment design. The unstable/stable manifold arcs that emanate from step-off locations that lie within a single revolution downstream/upstream from the step-off state associated with the outbound/inbound segment are utilized for the construction of the IO1Earth/EarthIO2 segment. This design choice narrows down the options offered by the manifolds of a QPO, as well as assists in constructing a bridging arc with short TOF that connects the segments that depart and arrive at the orbit. No such reduction in solution space is needed for manifolds associated with an intermediate periodic orbit. A pair of unstable and stable manifold arcs associated with the first and the second intermediate orbits is selected such that the states of the arcs that lie on the far side of the Earth have a minimal position and velocity discontinuity. A Poincaŕe map with hyperplane at $y = 0$ is employed to capture the manifold states that cross the far side of the Earth as illustrated for the unstable manifold arcs corresponding to an L_2 vertical orbit in fig. 33. Then, a K-Nearest Neighbors (KNN) algorithm is leveraged to identify the unstable and stable manifold arcs that have small position and velocity discontinuity, similar to the approach detailed by Pritchett [28] and LaFarge [34]. The search space of the algorithm is

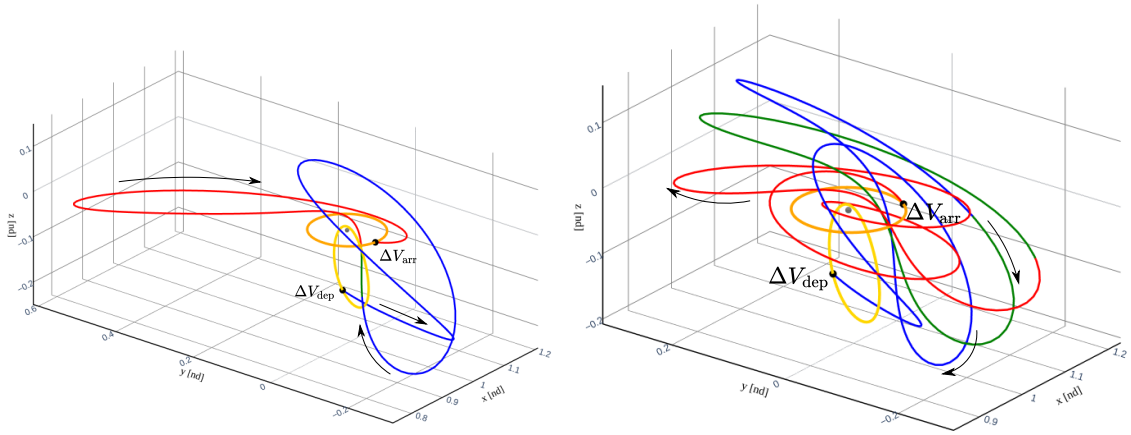

(a) Informed by an L_2 P2HO$_2$ orbit, $\Delta V_{\text{tot}} = \Delta V_{\text{dep}} + \Delta V_{\text{arr}}$ = 232.164 + 231.569 = 463.733 m/s, TOF = 45.314 days.

(b) Informed by an L_2 quasi-vertical orbit, $\Delta V_{\text{tot}} = \Delta V_{\text{dep}} + \Delta V_{\text{arr}}$ = 220.288 + 141.960 = 362.245 m/s, TOF = 82.448 days.

Fig. 32 Interior-type locally fuel-optimal transfers initiailzed by two feasible solution, figs. 28(b) and 31(a), that are characterized by an L_2 P2HO$_2$ and L_2 quasi-vertical orbit. The blue, green, and red colored portions of the full-state continuous trajectory are post-optimization remnants of the three colored arcs along the initial guess.

populated with the position and velocity components of the manifold states and the position components are scaled by a factor of 10. Thereafter, the L2 norm of the difference between the six components of the unstable and stable manifold states is utilized as the search criteria to deliver the candidates for the IO1Earth and EarthIO2 segments.

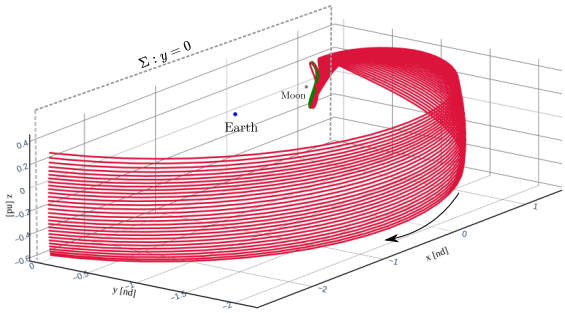

Fig. 33 Unstable manifolds (red) associated wih an L_2 vertical orbit (green) propagated till the first crossing of a Poincáre map at y=0 on the far side of the Earth.

The design of the bridging arcs is informed by the natural flow along an intermediate orbit. The segments that approach and depart an intermediate periodic orbit are linked via a bridging arc that is constructed through the strategy discussed in section III.C. The estimate of the time of flight of the arc is determined through eq. (49). Since the IO1Earth/EarthIO2 segment associated with an intermediate QPO is designed to lie in the immediate downstream/upstream of the outbound/inbound segment, the departing and approaching segments are straightforwardly constructed by bridging arc with an approximate TOF given by eq. (51).

The identified six segments are stitched together through a differential corrections scheme to reveal three maneuver exterior-type transfers. The corrections scheme is formulated to overcome the position and velocity discontinuity between all the segments, except for the velocity discontinuity between the IO1Earth and EarthIO2 segments. Additionally, the segments are constrained to be position continuous with the departure and arrival orbit. Hence, the three velocity discontinuities, between the departure orbit state and the first segment, IO1Earth and EarthIO2 segments, the last segment and arrival orbit state, are overcome via three impulsive maneuvers. The time of flight of the segments, as well as the departure and arrival orbit locations, are allowed to vary during the corrections process. The resultant geometries uncovered through the selected intermediate orbits are plotted in figs. 34(a), 35(a), 36(a) and 37(a). It is apparent from

the presented results that the solutions informed by intermediate QPOs result in lower maneuver cost options than the ones leveraging their underlying periodic orbits.

The locally fuel-optimal solutions are realized by optimizing the differentially corrected solutions with an objective function that minimizes $|\Delta V_{\text{dep}}|^2 + |\Delta V|^2 + |\Delta V_{\text{arr}}|^2$. The optimization scheme is a transcription of the described differential corrections scheme along with the defined objective function. The geometries uncovered by the optimization scheme with the solutions plotted in figs. 34(a), 35(a), 36(a) and 37(a) as the initial guesses are visualized in figs. 34(b), 35(b), 36(b) and 37(a). The interior-point method, IPOPT, does compute lower maneuver cost solutions for the four cases than the ones constructed through the differential corrections scheme. It is notable that the maneuver cost of the geometries derived from the QPOs are comparable to the cost of transfers designed by Vutukuri [27] by leveraging resonant orbits and tangential maneuvers, as well as to the cost of solutions determined by Muralidharan et al. [31] through the stretching directions associated with the departure and arrival orbits. The proposed framework that incorporates QPOs as an option provides a modular and systematic approach to design low-cost transfer pathways between stable periodic orbits.

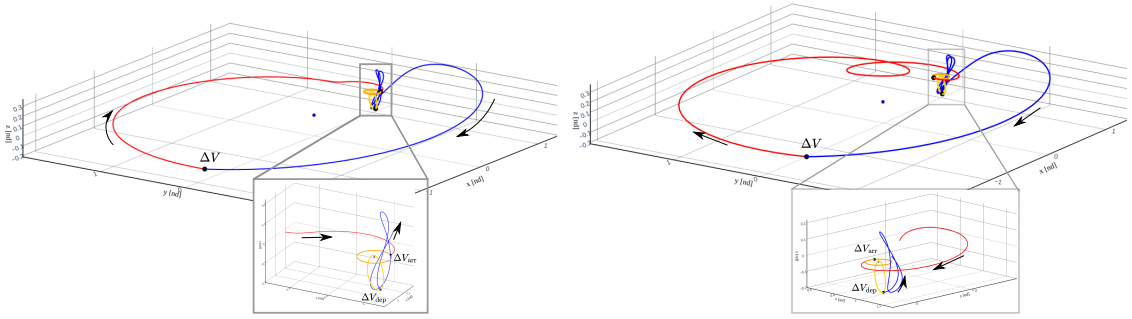

(a) Differentially corrected transfer, $\Delta V_{\text{tot}} = \Delta V_{\text{dep}} + \Delta V + \Delta V_{\text{arr}} = 273.622 + 203.583 + 425.671 = 902.876$ m/s, TOF = 99.844 days.

(b) Optimized transfer, $\Delta V_{\text{tot}} = \Delta V_{\text{dep}} + \Delta V + \Delta V_{\text{arr}} = 261.105 + 108.795 + 153.828 = 523.729$ m/s, TOF = 115.161 days

Fig. 34 Exterior-type differentially corrected and optimized transfers informed by an L_2 vertical orbit and a 3:4 RPO. The outbound segment from an NRHO to the far side of the Earth (blue) requires a maneuver to overcome the velocity discontinuity with the inbound segment from the far side of the Earth to a DRO (red).

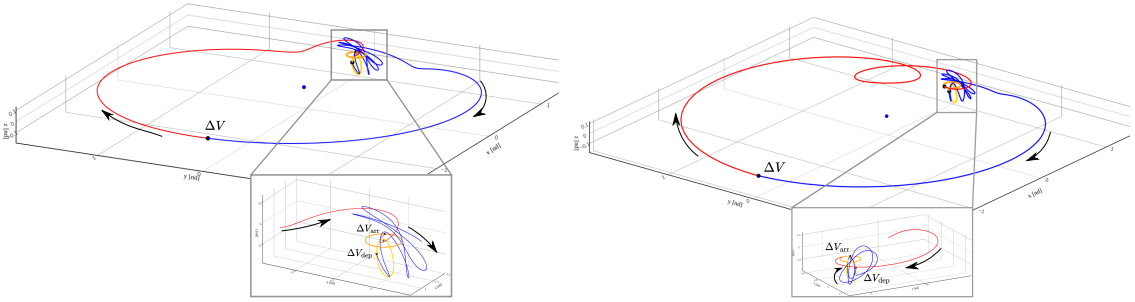

(a) Differentially corrected transfer, $\Delta V_{\text{tot}} = \Delta V_{\text{dep}} + \Delta V + \Delta V_{\text{arr}} = 130.789 + 16.231 + 472.628 = 619.649$ m/s, TOF = 127.534 days.

(b) Optimized transfer, $\Delta V_{\text{tot}} = \Delta V_{\text{dep}} + \Delta V + \Delta V_{\text{arr}} = 86.254 + 105.437 + 58.414 = 250.106$ m/s, TOF = 135.018 days.

Fig. 35 Exterior-type differentially corrected and optimized transfers informed by an L_2 quasi-vertical orbit and a 3:4 RPO. The outbound segment from an NRHO to the far side of the Earth (blue) requires a maneuver to overcome the velocity discontinuity with the inbound segment from the far side of the Earth to a DRO (red).

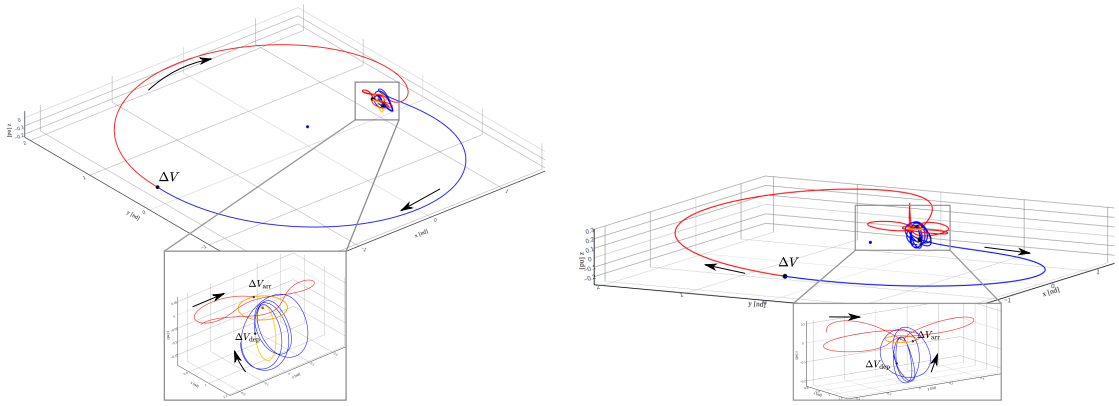

(a) Differentially corrected transfer, $\Delta V_{tot} = \Delta V_{dep} + \Delta V + \Delta V_{arr}$ = 103.549 + 88.261 + 366.775 = 558.585 m/s, TOF = 150.697 days.

(b) Optimized transfer, $\Delta V_{tot} = \Delta V_{dep} + \Delta V + \Delta V_{arr}$ = 62.064 + 17.768 + 113.701 = 193.534 m/s, TOF = 174.708 days.

Fig. 36 Exterior-type differentially corrected and optimized transfers informed by an L_2 P2HO$_2$ orbit and a DPO. The outbound segment from an NRHO to the far side of the Earth (blue) requires a maneuver to overcome the velocity discontinuity with the inbound segment from the far side of the Earth to a DRO (red).

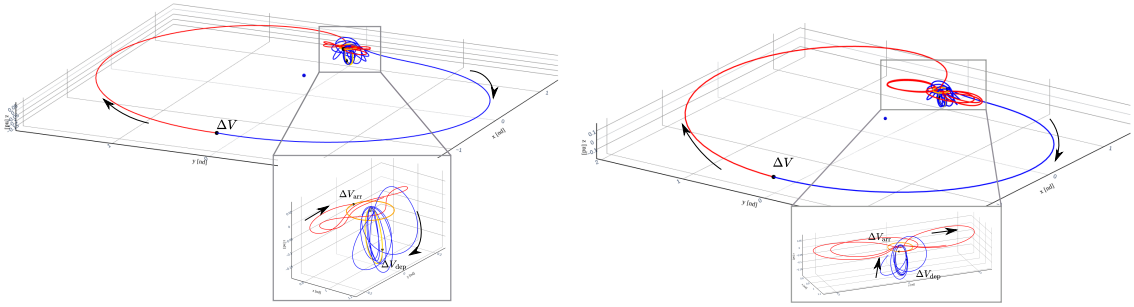

(a) Differentially corrected transfer, $\Delta V_{tot} = \Delta V_{dep} + \Delta V + \Delta V_{arr}$ = 20.759 + 73.338 + 400.426 = 494.524 m/s, TOF = 179.871 days.

(b) Optimized transfer, $\Delta V_{tot} = \Delta V_{dep} + \Delta V + \Delta V_{arr}$ = 6.033 + 82.995 + 29.289 = 118.318 m/s, TOF = 220.296 days.

Fig. 37 Exterior-type differentially corrected and optimized transfers informed by an L_2 quasi-P2HO$_2$ orbit and a DPO. The outbound segment from an NRHO to the far side of the Earth (blue) requires a maneuver to overcome the velocity discontinuity with the inbound segment from the far side of the Earth to a DRO (red).

IV. Transfers Between Unstable Periodic Orbits in the Same Family

The design of low maneuver cost transfer pathways with reasonable time of flights between spatial periodic orbits in the same Lagrange point family that possess stable and unstable invariant manifolds may be challenging due to the difference in their energy levels. Even if the hyperbolic manifolds associated with the type of periodic orbits under consideration are useful, due to the difference in their energy levels, the manifolds might not uncover locally fuel-optimal transfer options with feasible flight times. There are multiple classes of solutions to this problem that are described by various investigations. Davis et al. leverage the invariant manifolds associated with the departure and arrival periodic orbits to construct mass optimal solutions with long flight times. The geometries uncovered by Davis et al. make multiple revolutions around the libration point and the second primary. Prado et al., as well as Pritchett et al. use the concept of orbit chaining with multiple members of the same family to construct low-thrust interior-type multiple-revolution transfers [28, 29]. McCarthy incorporates a QPO torus that crosses the departure and arrival orbits in the design process to produce a two-maneuver interior-type multiple-revolution solution [8]. Bell relies on primer vector theory to construct two and three-maneuver interior-type direct transfers, i.e., transfers that do not complete a revolution around the originating Lagrange point of the periodic orbit family [35]. Gómez et al. construct similar solutions as Bell by employing the Floquet modes of the departure and arrival orbits to inform the design process [11].

The numerous classes of transfers establish feasible solutions with varied desirable characteristics.

A proposed framework leverages the unstable manifolds associated with QPOs to extend the known solutions to the problem scenario. Additionally, the constructed solutions are compared with the locally fuel-optimal geometries, and the initial guess for the optimal transfers is obtained from the methodology described by Gómez et al. [11]. The proposed strategy uncovers *1-paramter* family of two-maneuver direct transfers for select departure and arrival orbit. The framework is illustrated for transfers between L_1 northern halo orbits in the Earth-Moon system, plotted in fig. 38(a). It is notable that the out-of-plane amplitude (A_z, z-component of the apolune state) of the L_1 halo orbits increase monotonically and there are multiple tangent bifurcations across the family as depicted in fig. 38(b). Hence, the L_1 halo orbits may be alternatively represented by their A_z values. More specifically, transfers from a departure halo orbit with A_z = 10,000 km to halo orbits with higher A_z values are constructed through the two strategies and then compared. It is also noted that the fuel optimal transfers and their initial guess illuminate a linear relationship between the maneuver cost and A_z value of the arrival orbits that are even remarked by Bell [35] and Gómez et al. [11]. The QPO derived pathways enhance the two-maneuver direct transfer options uncovered by the optimization strategy.

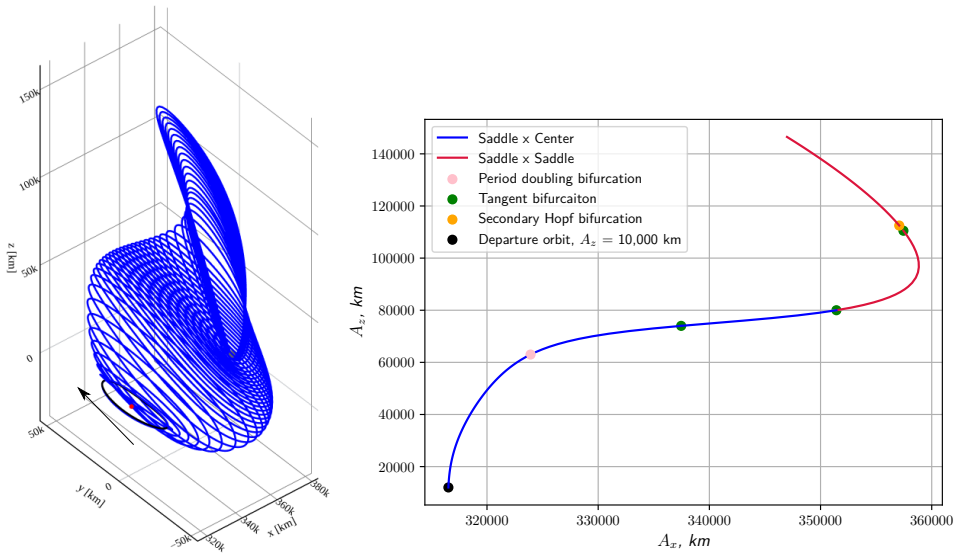

(a) Configuration Space **(b) A_x vs A_z hodograph and stability information**

Fig. 38 Configuration plot and A_x vs A_z hodograph of the L_1 northern halo orbits in the Earth-Moon system. The orbits are marked by their stability characteristics in the hodograph and the A_z = 10,000 km departure orbit appears in black in the configuration plot.

A. Locally Fuel-Optimal Transfers

Locally fuel-optimal transfers are devised through initial guesses identified via stable and along orbit Floquet modes of the chosen departure and arrival orbits, as described by Gómez et al. [11]. To elucidate the initial guess generation strategy, consider two closely spaced unstable orbits of the same family. An arbitrary two-maneuver direct transfer ($\Delta\bar{v}_1$, $\Delta\bar{v}_2$) connects these orbits, as illustrated in fig. 39. The $\bar{x}^{\text{dep}}_{\tau_1}$ and $\bar{x}^{\text{arr}}_{\tau_2}$ states in the schematic correspond to states on the departure and arrival orbit. The two states are τ_1 and τ_2 propagation time downstream of their respective orbits' states that cross the $\hat{x} - \hat{z}$ plane with $\dot{y} > 0$, and it is assumed that $\tau_1 < \tau_2$. Since the two orbits are near each other the $\bar{x}^{\text{dep}}_{\tau_2}$ and $\bar{x}^{\text{arr}}_{\tau_2}$ states are similar. Gomez et al. propose that the fuel-optimal transfers are governed by the stable and the along orbit Floquet modes of arrival orbit states. Hence, the post-second maneuver transfer state is expressed as $\bar{x}^{\text{arr}}_{\tau_2} + \gamma_s \bar{e}^{\text{arr}}_s(\tau_2) + \gamma_o \bar{e}^{\text{arr}}_o(\tau_2)$, where $\bar{e}^{\text{arr}}_s(\tau_2)$ and $\bar{e}^{\text{arr}}_o(\tau_2)$ denote the stable and along orbit Floquet modes of the arrival orbit at τ_2 and are computed through the procedure described in section II.B. The γ_s and γ_o are the linear coefficients of the two Floquet modes. The transfer is alternatively expressed in terms of the two maneuvers,

$$\bar{x}^{\text{dep}}_{\tau_2} + \mathbf{\Phi}(\tau_2, \tau_1)[\bar{0}\ \Delta\bar{v}_1]^T + [\bar{0}\ \Delta\bar{v}_2]^T = \bar{x}^{\text{arr}}_{\tau_2} + \gamma_s \bar{e}^{\text{arr}}_s(\tau_2) + \gamma_o \bar{e}^{\text{arr}}_o(\tau_2) \tag{52}$$

where, $\mathbf{\Phi}(\tau_2, \tau_1)$ represents the STM that maps the impact of linear variations on $\bar{x}^{\text{dep}}_{\tau_1}$ to $\bar{x}^{\text{dep}}_{\tau_2}$ state. The transfer representation on the left is derived by propagating the post-first maneuver state, $\bar{x}^{\text{dep}}_{\tau_1} + [\bar{0}\ \Delta\bar{v}_1]^T$, till τ_2 time to obtain the $\bar{x}^{\text{dep}}_{\tau_2} + \mathbf{\Phi}(\tau_2, \tau_1)[\bar{0}\ \Delta\bar{v}_1]^T$ state and then adding the second maneuver. The Floquet mode coefficients' values are sought to minimize total maneuver cost and satisfy eq. (52), providing an initial guess.

The Floquet mode-constrained initial guess design strategy, given by eq. (52), is linearized to identify locally optimal departure and arrival locations that result in locally fuel-optimal transfers and to generalize the formulation for different arrival orbits. A parameter β is introduced to represent the periodic orbits in their continuous *1-parameter* family. Consequently, a departure orbit is denoted by β and a nearby arrival orbit is represented as $\beta + \Delta\beta$. Thus, the eq. (52) is rewritten in terms of β as,

$$\bar{x}^{\beta}_{\tau_2} + \mathbf{\Phi}(\tau_2, \tau_1)[\bar{0}\ \Delta\bar{v}_1]^T + [\bar{0}\ \Delta\bar{v}_2]^T = \bar{x}^{(\beta+\Delta\beta)}_{\tau_2} + \gamma_s \bar{e}^{(\beta+\Delta\beta)}_s(\tau_2) + \gamma_o \bar{e}^{(\beta+\Delta\beta)}_o(\tau_2) \tag{53}$$

For a small $\Delta\beta$ value, the above equation is expanded as,

$$\begin{aligned} \cancel{\bar{x}^{\beta}_{\tau_2}} + \mathbf{\Phi}(\tau_2, \tau_1)[\bar{0}\ \Delta\bar{v}_1]^T + [\bar{0}\ \Delta\bar{v}_2]^T = \cancel{\bar{x}^{\beta}_{\tau_2}} + \frac{\partial \bar{x}^{\beta}_{\tau_2}}{\partial \beta}\Delta\beta + O[(\Delta\beta)^2] \\ + \gamma_s \left(\bar{e}^{\beta}_s(\tau_2) + \frac{\partial \bar{e}^{\beta}_s(\tau_2)}{\partial \beta}\Delta\beta \right) \\ + \gamma_o \left(\bar{e}^{\beta}_o(\tau_2) + \frac{\partial \bar{e}^{\beta}_o(\tau_2)}{\partial \beta}\Delta\beta \right) \end{aligned} \tag{54}$$

The partial derivative terms, $\frac{\partial \bar{e}^{\beta}_s(\tau_2)}{\partial \beta}$ and $\frac{\partial \bar{e}^{\beta}_o(\tau_2)}{\partial \beta}$, are neglected as for $O[\gamma_{s/o}] = O[\Delta\beta]$ their contribution is $O[(\Delta\beta)^2]$. The simplified form of eq. (54) is written as,

$$\mathbf{\Phi}(\tau_2, \tau_1)[\bar{0}\ \Delta\bar{v}_1]^T + [\bar{0}\ \Delta\bar{v}_2]^T = \left(\frac{\partial \bar{x}^{\beta}_{\tau_2}}{\partial \beta} + \frac{\gamma_s}{\Delta\beta}\bar{e}^{\beta}_s(\tau_2) + \frac{\gamma_o}{\Delta\beta}\bar{e}^{\beta}_o(\tau_2) \right) \Delta\beta \tag{55}$$

All the terms in the above equation are a function of the departure orbit, β, and the information about the arrival orbit is solely encapsulated by $\Delta\beta$. The solutions to the equation for a fixed value of $\Delta\beta$ may be extrapolated for a range of $\Delta\beta$ values corresponding to nearby arrival orbits. It is straightforward to realize that for a fixed departure orbit and $\Delta\beta$ value, the formulated *6-dimensional* expression in eq. (55) comprise of ten parameters: $\Delta\bar{v}_1$, $\Delta\bar{v}_2$, τ_1, τ_2, γ_s and γ_o. Since the defined problem is underconstrained, values of γ_s and γ_o are computed for fixed τ_1 and τ_2 values that result in the minimum total maneuver cost. An interior point method, IPOPT [33], is employed to ascertain the values of γ_s and γ_o that minimizes an objection function defined as $|\bar{v}_1|^2+|\bar{v}_2|^2$. The optimization process is repeated for a range of τ_1 and τ_2 values to uncover the optimization landscape of the problem to enable the recognition of initial guesses to local solution basins.

The outlined initial guess strategy is leveraged to construct transfers from the selected departure orbit to orbits with higher A_z values. For the L_1 halo orbit family, the β parameter is defined as the A_z value of the orbits. For the departure L_1 halo orbit, $\beta = A_z$ = 10,000 km, the solutions to the formulated equation, eq. (55), are determined for $\Delta\beta$ = 1 [nd]. The τ_1 and τ_2 values are cast as the mean anomaly of the orbit and represented as θ_{τ_1} and θ_{τ_2} in degrees. The departure location, θ_{τ_1}, is varied from 0° to 360° and the corresponding arrival location, θ_{τ_2}, is varied from θ_{τ_1} to $\theta_{\tau_1} + 360°$ to compute the optimization landscape. The resultant performance surface for the initial guess is represented on a heat map in fig. 40, where the solutions are colored by the total maneuver cost in m/s per 1,000 km $\Delta\beta$. The initial guess for the time of flight of the transfers is approximated as the difference between τ_1 and τ_2 values corresponding to their θ_{τ_1} and θ_{τ_2} values. It is apparent from the heat map that multiple solution basins exist for the problem, so the focus is narrowed down to solutions with shorter TOF as marked by the red curve in fig. 40. Bell and Gomez et al. identify that the maneuver magnitudes of the two maneuvers of the optimal transfers are similar for transfers between L_1 halo orbits in the Sun-Earth system [11, 35]. This additional information is leveraged to reduce the options in a local basin to one with comparable maneuver costs of the first and second maneuver, marked by pink dots in fig. 40. A solution represented by a pink dot in the basin A and B as depicted in the heat map inform the design of locally optimal transfers.

The locally fuel-optimal transfers are constructed by feeding selected initial guesses to an optimization scheme with an objection function that minimizes $|\bar{v}_1|^2+|\bar{v}_2|^2$. The optimization scheme delivers a transfer that is position continuous

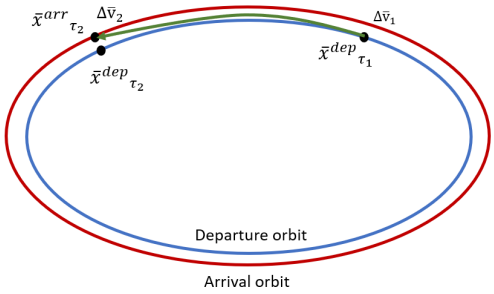

Fig. 39 Initial guess design strategy schematic

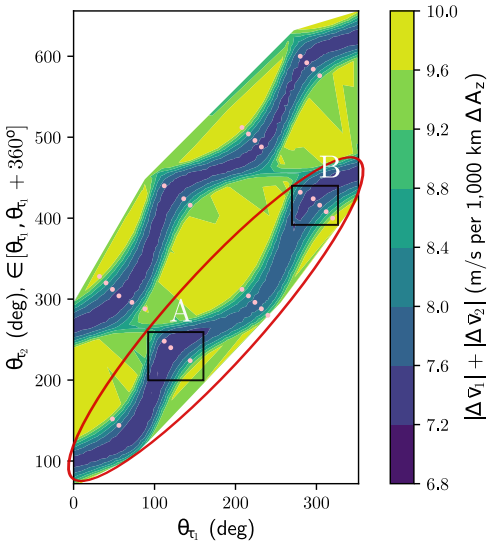

Fig. 40 Optimization landscape for the initial guesses from A_z = 10,000 km halo orbit. Two solution basins of interest are marked as A and B.

with the departure and arrival orbit, and locally fuel-optimal. The time of flight, as well as the departure and arrival orbit locations, are allowed to vary during the optimization process. To illustrate the efficacy of the described initial guess generation strategy, two guesses that correspond to the two different solution basins as depicted in fig. 40 are optimized for an arrival orbit with A_z value of 20,000 km, which corresponds to a $\Delta\beta$ value of 10,000 km = 0.02601 [nd]. The initial guess and the optimized transfer geometries are visualized in fig. 41, and the departure and arrival locations of the optimized transfers are plotted on the heat map representation in fig. 42. It is evident from fig. 41 that the initial guess constructed through the described strategy well approximates the geometries of the local optimal transfers.

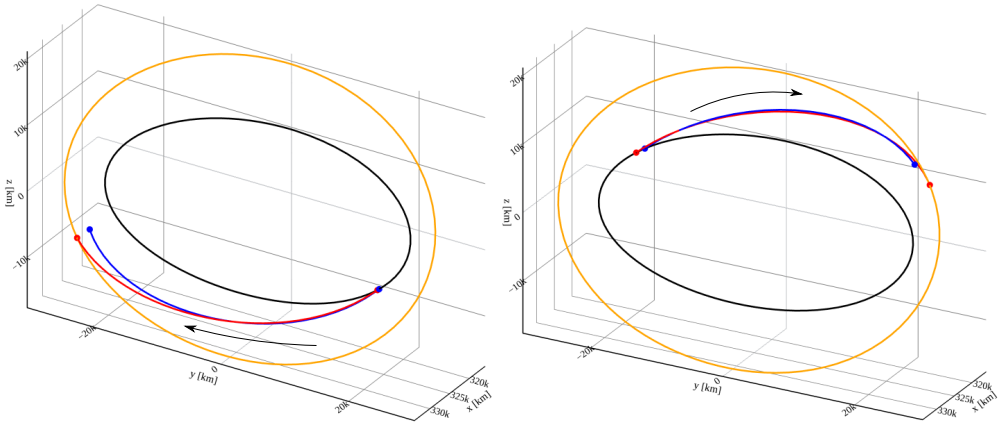

(a) Solution basin A **(b) Solution basin B**

Fig. 41 Initial guess (blue) and optimized transfer (red) geometries to traverse from a halo orbit with A_z = 10,000 km (black) to A_z = 20,000 km (orange)

The identified initial guess in solution basin B is extrapolated for a range of $\Delta\beta$ values to design transfers from the halo orbit with A_z = 10,000 km to halo orbits with higher A_z values. The optimized pathways designed via the selected initial guess are plotted in fig. 43, and the maneuver costs approximated from the initial guess and the theoretical min ΔV values, as well as cost of the locally optimal transfers, are presented in fig. 44. Additionally, the maneuver magnitudes

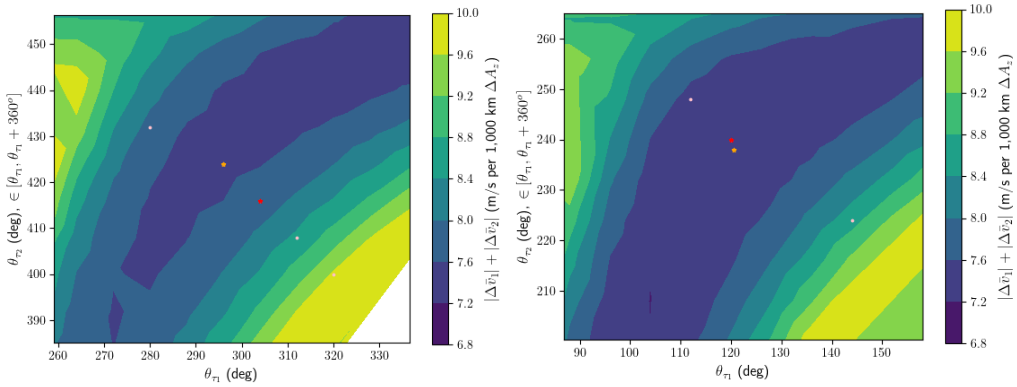

(a) Solution basin A **(b) Solution basin B**

Fig. 42 Zoomed-in view of the optimization landscape presented in fig. 42 that depicts the initial guess (red) and optimized transfer (orange) that connects halo orbit with A_z = 10,000 km to 20,000 km

of the two maneuvers for the optimal transfers are depicted in fig. 45. It is evident from fig. 44 that the cost of initial guess and optimal transfers are higher than the TMDV values, which is the expected behavior, and the initial guess well predicts the cost of optimal transfers up till the halo orbit with $A_z \approx 75{,}000$ km. The linear relationship between the maneuver cost and the difference in the A_z values of the departure and arrival orbits, as remarked by Bell [35] and Gomez et al. [11], is notable in fig. 44 for transfers from the A_z = 10,000 km to $A_z \lessapprox 75{,}000$ km. The change in the linear relationship between the total maneuver cost and A_z for halo orbit with A_z value greater than $\approx 75,000$ km may be attributed to the distinct change in the geometry of the halo orbits as well the presence of multiple tangent bifurcations as depicted in fig. 45. Due to the presence of multiple tangent bifurcations for the part of the halo orbit family where the members evolve more rapidly in A_x than in A_z may go through a fundamental change in the direction of stable and along orbit Floquet modes that would require a modification to the linear approximation made in eq. (54) to more accurately approximate the maneuver cost for the arrival halo orbits with A_z values greater than $\approx 75{,}000$ km. Nonetheless, the outlined initial guess strategy serves as a good first estimation of the two maneuvers and flight times from the selected departure orbit to arrival orbits with similar characteristics. This initial guess generation technique is extendable to the design of transfers to arrival orbits with A_z values smaller than the departure orbit, and the symmetry of the CR3BP model can be exploited to generate transfers that evolve from the arrival orbits to the departure orbit, as well as for transfers between L_1 southern halo orbit counterparts of the presented northern halo orbits. The optimal transfers constructed from the departure to a few arrival orbits are compared with the transfer trajectories derived from QPOs.

B. Quasi-Periodic Orbits Informed Transfers

The unstable manifolds associated with QPOs are leveraged to design families of two-maneuver direct transfers between unstable orbits in the same orbit family. The design of the transfers initiates by selecting candidate QPOs and identifying their corresponding manifold arcs that cross the vicinity of the departure and arrival orbits. Then a differential corrections scheme is employed to realize two-maneuver direct transfers with the key constraint that each transfer is a segment of an unstable manifold arc corresponding to a QPO. The initial guess generation strategy and differential corrections procedure are an extension of the methodologies described in section III.A. For the direct comparison of QPO-derived transfers with the fuel-optimal transfers, presented in section IV.A, the QPOs are selected to possess the same JC value as their optimal transfer counterpart generated for a pair of departure and arrival orbit.

The potential candidates for the unstable manifold arcs that cross the vicinity of a departure and an arrival orbit are identified through an events function that leverages a continuous representation of the two orbits. The continuous representation of departure and arrival orbits are generated through the strategy described by Jain [21]. For a selected QPO, the associated unstable manifold arcs are approximated through the strategy described in section II.C. Then by employing the events function, the unstable manifold arcs that have a position discontinuity with a deparute orbit state of less than 5000 km are recorded. This procedure is repeated to identify unstable manifold arcs that reach the proximity of an arrival orbit. Thereafter, the manifold arcs that are common to the list of manifold arcs that cross in the vicinity of

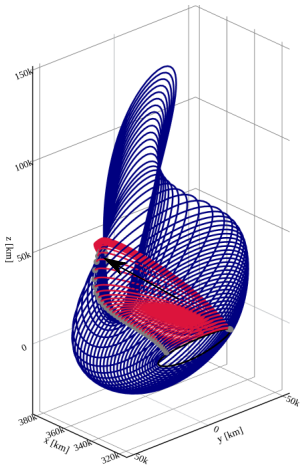

Fig. 43 Locally fuel-optimal transfers (red) from a halo orbit with A_z = 10,000 km (black) to orbits with higher A_z values blue.

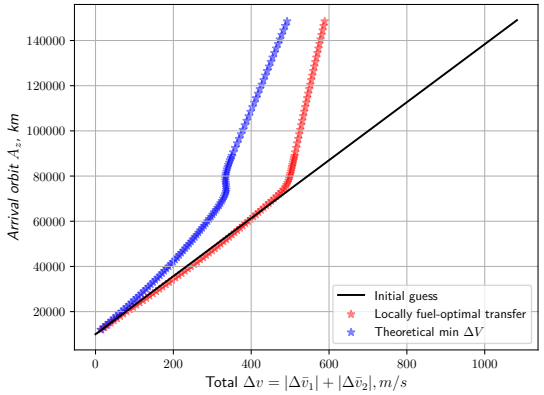

Fig. 44 The total maneuver cost predicted by the initial guess (black) and theoretical minimum ΔV (blue), as well as the cost of locally optimal solutions (red) are plotted with respect to the A_z values of the arrival orbits.

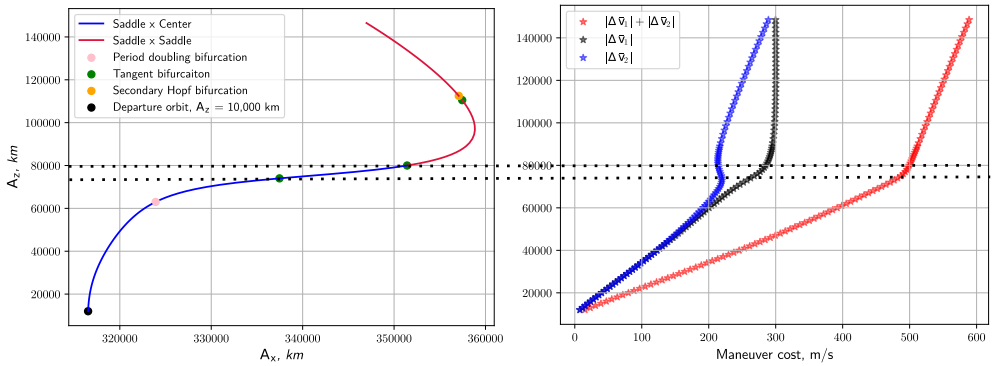

Fig. 45 The linear relationship between the total maneuver cost (red stars) as well as for the two maneuvers (blue and black starts) with the A_Z value of the arrival orbits changes at orbits that evolve more rapidly in A_x than in A_z and undergo multiple tangent bifurcations as identified by the black colored dashed lines.

the departure and arrival orbits are selected as the initial guesses for the transfer design problem.

An identified initial guess is corrected through a differential corrections procedure to realize an unstable manifold arc associated with a QPO that is position continuous with the departure and arrival orbit. The differential corrections scheme is formulated as a Newton-Raphson method. The design ($\bar{X}$) and constraint ($\bar{F}(\bar{X})$) vectors for the corrections scheme are defined as,

$$\bar{X} = \begin{bmatrix} T_{\text{dep}} \\ T_{\text{arr}} \\ \tau_{\text{dep}} \\ \tau_{\text{arr}} \\ \tau_{\text{qpo}} \\ \Omega_{\rho^0} \end{bmatrix}; \quad \bar{F}(\bar{X}) = \begin{bmatrix} u x^{T_{\text{dep}}}_{\tau_{\text{qpo}},\Omega_{\rho^0}} - x^{\tau_{\text{dep}}}_{\text{dep}} \\ u y^{T_{\text{dep}}}_{\tau_{\text{qpo}},\Omega_{\rho^0}} - y^{\tau_{\text{dep}}}_{\text{dep}} \\ u z^{T_{\text{dep}}}_{\tau_{\text{qpo}},\Omega_{\rho^0}} - z^{\tau_{\text{dep}}}_{\text{dep}} \\ u x^{T_{\text{arr}}}_{\tau_{\text{qpo}},\Omega_{\rho^0}} - x^{\tau_{\text{arr}}}_{\text{arr}} \\ u y^{T_{\text{arr}}}_{\tau_{\text{qpo}},\Omega_{\rho^0}} - y^{\tau_{\text{arr}}}_{\text{arr}} \\ u z^{T_{\text{arr}}}_{\tau_{\text{qpo}},\Omega_{\rho^0}} - z^{\tau_{\text{arr}}}_{\text{arr}} \end{bmatrix} \tag{56}$$

where, τ_{qpo} and Ω_{ρ^0} represent the step-off state corresponding to an unstable manifold arc, specifically, τ_{qpo} is the propagation time along a QPO from an initial invariant curve to the invariant curve on which the step off-state lies and

Ω_{ρ^0} is the modified latitudinal angle associated with the step-off state. The T_{dep} and T_{arr} denote propagation times along the unstable manifold arc from an initial manifold state to the manifold states that crosses the departure and arrival orbit, respectively, and it is assumed that $T_{\text{dep}} < T_{\text{arr}}$. Additionally, τ_{dep} and τ_{arr} represent the propagation times along the departure and arrival orbit from some predetermined initial states on the orbits to the orbit states that connect with the unstable manifold arc. The constraint vector comprises of the position components of two states on the unstable manifold arc: ${}_u\bar{x}^{T_{\text{dep}}}_{\tau_{\text{qpo}},\Omega_{\rho^0}}$ and ${}_u\bar{x}^{T_{\text{arr}}}_{\tau_{\text{qpo}},\Omega_{\rho^0}}$, as well as the position components of a departure orbit state, $\bar{x}^{\tau_{\text{dep}}}_{\text{dep}}$, and an arrival orbit state, $\bar{x}^{\tau_{\text{arr}}}_{\text{arr}}$. Consequently, the corrected unstable manifold arc originating from a step-off state given by τ_{qpo} and Ω_{ρ^0} comprises of a manifold state, ${}_u\bar{x}^{T_{\text{dep}}}_{\tau_{\text{qpo}},\Omega_{\rho^0}}$, that has the same position components as a departure orbit state, $\bar{x}^{\tau_{\text{dep}}}_{\text{dep}}$, as well as another manifold state, ${}_u\bar{x}^{T_{\text{arr}}}_{\tau_{\text{qpo}},\Omega_{\rho^0}}$, that is further downstream from the ${}_u\bar{x}^{T_{\text{dep}}}_{\tau_{\text{qpo}},\Omega_{\rho^0}}$ state, has the same position components as an arrival orbit state, $\bar{x}^{\tau_{\text{arr}}}_{\text{arr}}$, as depicted in the fig. 46. The presented corrections scheme is fully-constrained, hence, the *3-dimensional* unstable manifold associated with a QPO results in locally unique solutions. However, since the QPOs exist as a constant energy family, a continuation algorithm is leveraged to extend the locally unique solutions to local *1-parameter* families of solutions with a common JC value.

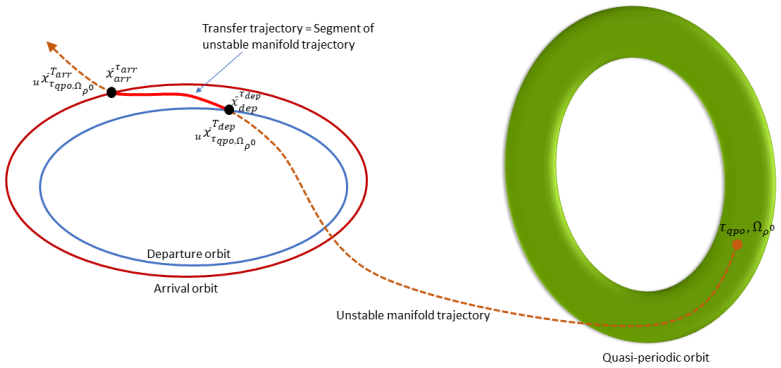

Fig. 46 Schematic of a transfer trajectory between two periodic orbits derived from a quasi-periodic orbit

The outlined initial guess generation technique and differential corrections procedure are employed to design transfers from the selected L_1 northern halo orbit with A_z value of 10,000 km to halo orbits with larger A_z values. The L_1 quasi-halo orbits are selected as the QPOs to construct the transfers. The pathways from halo orbit with A_z = 10,000 km to 20,000 km are constructed through the quasi-halo orbits with the same JC value as the optimal transfer, as presented in fig. 41(b). The *1-parameter* family of transfers realized through the quasi-halo orbits and the optimal transfer are plotted in fig. 47, where the QPO-derived solutions are colored by their total maneuver costs. Additionally, the costs of the transfers constructed through the two strategies described are represented in fig. 50. Similarly, the transfers from the selected departure orbit to orbits with A_z = 42,000 km and 50,000 km along with their fuel-optimal counterparts are plotted in figs. 48 and 49 and their costs are also provided in fig. 50. It is apparent from figs. 47 to 49 that the transfers designed via the two strategies for the three arrival orbits possess similar geometries as the solutions depart and arrive at the orbits in the same vicinity. The *1-parameter* QPO-derived pathways expand the number of transfer options identified by the locally unique fuel-optimal solutions to a range of departure and arrival locations. Additionally, the maneuver costs associated with the transfers informed by quasi-halos are comparable to the optimal geometries as evident in fig. 50. Hence, quasi-periodic orbits assist in uncovering a family of transfers that have comparable geometries and maneuver costs as the fuel-optimal solutions.

V. Concluding Remarks

Quasi-periodic orbits enhance the transfer options that link different types of periodic orbits. The proposed systematic frameworks reduce the complexity of employing the *5-dimensional* manifolds associated with the *2-parameter* quasi-periodic orbits, modeled through CR3BP, to design transfers between stable, as well as unstable periodic orbits. The nearly/marginally stable periodic orbits that lack useful hyperbolic invariant manifolds are linked via two maneuver interior-type and three maneuver exterior-type transfer trajectories. An L_2 9:2 NRHO and a DRO are employed to illustrate the framework that addresses the challenge of constructing transfers between stable orbits. The design of

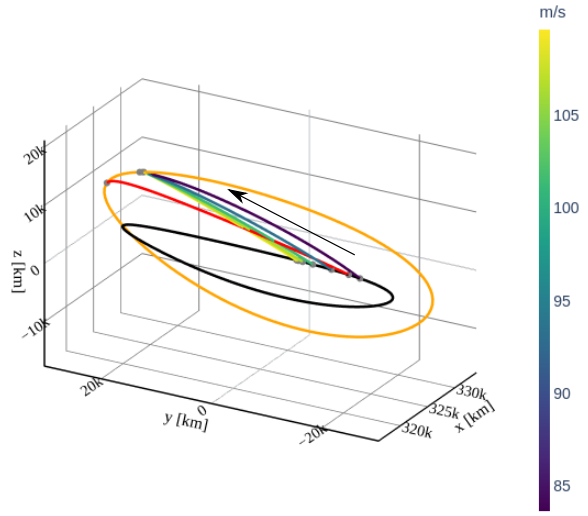

Fig. 47 QPO-derived transfers (color bar) and locally fuel-optimal transfer (red) from halo orbit A_z = 10,000 (black) to 20,000 (orange)

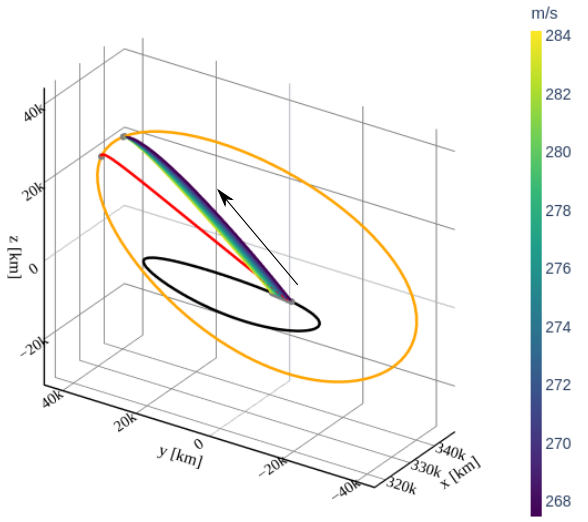

Fig. 48 QPO-derived transfers (color bar) and locally fuel-optimal transfer (red) from halo orbit A_z = 10,000 (black) to 42,000 (orange)

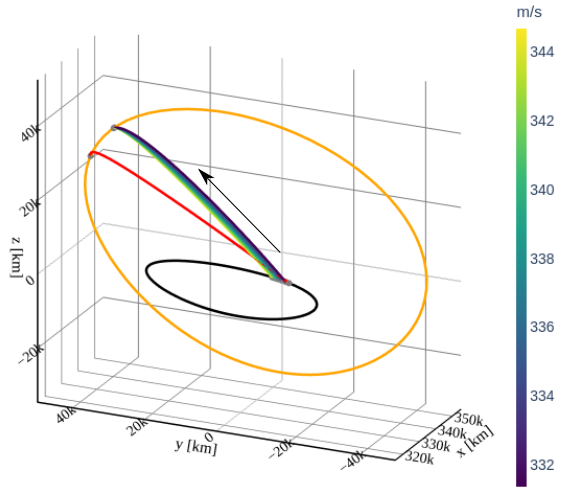

Fig. 49 QPO-derived transfers (color bar) and locally fuel-optimal transfer (red) from halo orbit A_z = 10,000 (black) to 50,000 (orange)

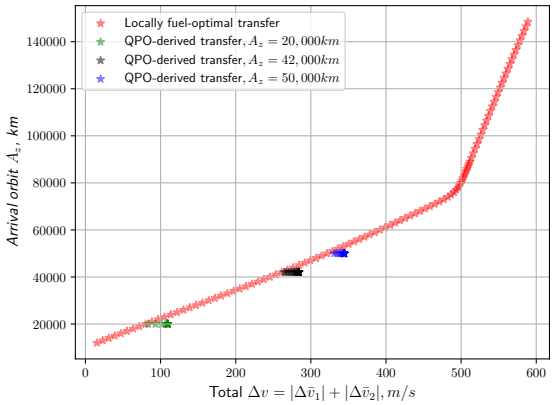

Fig. 50 Total maneuver cost of locally optimal solutions (red) and transfers informed by QPOs (green, black, and blue) are plotted with respect to the A_z values of the arrival orbits

the two types of transfers is decomposed into the construction of various segments that are informed by the natural flow, as well as the stable and unstable manfiolds associated with intermediate orbits. It is identified that the selected intermediate QPOs assist in realizing a greater number of transfer geometries with lower maneuver costs than those derived from their underlying periodic orbits. For the case of transfers between unstable orbits within the same orbit family, two distinct strategies are described and their respective solutions are compared. Locally fuel-optimal transfers are constructed between unstable orbits by leveraging an initial guess generation strategy proposed by Gómez et al. [19]. The optimal transfers between L_1 halo orbits reveal a linear relationship between the total maneuver cost and the difference in out-of-plane amplitude of the departure and arrival orbits. The second strategy employs the unstable manifolds associated with QPOs to uncover *1-parameter* families of transfers between L_1 halo orbits. A comparison of outcomes from both strategies indicates that, although the *1-parameter* QPO-derived transfers are not locally fuel-optimal, their geometries and transfer costs are comparable. Importantly, the QPO-informed solutions contribute to

the expansion of known transfer options, linking a greater range of departure and arrival locations. Quasi-periodic orbits and their associated stable/unstable manifolds uncover families of transfer options between periodic orbits of different types that may be infeasible to derive from other dynamical structures.

Appendix

Maneuver costs and time of flights of inbound and outbound segments constructed via intermediate periodic orbit to inform the design of tranfers between an L_2 NRHO and a DRO as detailed in section III.

Table 3 Maneuver costs and times of flight of the three transfer options, depicted in fig. 23(a), constructed with an L_2 vertical orbit as the intermediate orbit.

Transfer arc	$\Delta V_{\mathbf{arr}}$ (m/s)	**TOF** (days)
1	644.335	19.690
2	638.378	17.052
3	535.494	29.901

Table 4 Maneuver costs and times of flight of the inbound transfer options, depicted in fig. 23(b), constructed with an L_2 P2HO$_2$ orbit as the intermediate orbit.

Transfer arc	$\Delta V_{\mathbf{arr}}$ (m/s)	**TOF** (days)
1	669.800	27.708
2	602.450	28.380

Table 5 Maneuver costs and times of flight of the two transfer options, depicted in fig. 24(a), constructed with a planar 3:4 RPO as the intermediate orbit.

Transfer arc	$\Delta V_{\mathbf{arr}}$ (m/s)	**TOF** (days)
1	442.657	13.097
2	442.734	12.417

Table 6 Maneuver costs and times of flight of the two transfer options, depicted in fig. 24(b), constructed with a DPO as the intermediate orbit.

Transfer arc	$\Delta V_{\mathbf{arr}}$ (m/s)	**TOF** (days)
1	366.728	20.057
2	653.222	29.452

Table 7 Maneuver costs and times of flight of the two transfer options, depicted in fig. 25(a), constructed with an L_2 vertical orbit as the intermediate orbit.

Transfer arc	$\Delta V_{\mathbf{dep}}$ (m/s)	**TOF** (days)
1	275.097	15.278
2	197.810	30.879

Table 8 Maneuver costs and times of flight of the outbound transfer options, depicted in fig. 25(b), constructed with an L_2 P2HO$_2$ orbit as the intermediate orbit.

Transfer arc	$\Delta V_{\mathbf{dep}}$ (m/s)	**TOF** (days)
1	119.847	26.813
2	103.394	30.331

Acknowledgments

The authors thank the Purdue University College of Engineering for facilities and financial support. The authors recognize and appreciate valuable discussions with Dr. Brian McCarthy, Dr. Nicholas LaFarge, Beom Park, Dale Williams, Mitch Dominquez, and the rest of the members of Purdue's Multi-Body Dynamics Research Group for insight concerning the quasi-periodic orbits, Floquet theory and optimization schemes.

References

[1] "NASA strategic Plan 2022," , Mar 2022. URL https://www.nasa.gov/sites/default/files/atoms/files/2022_nasa_strategic_plan.pdf.

[2] "ISRO Chandrayaan-3," , 2023. URL https://www.isro.gov.in/Chandrayaan3_New.html.

[3] "ispace HAKUTO-R," , Jul 2020. URL https://ispace-inc.com/hakuto-r/eng/.

[4] "Inutive Machines IM-1," , 2022. URL https://www.intuitivemachines.com/im-1.

[5] "JAXA Lunar polar exploration mission," , 2020. URL http://www.exploration.jaxa.jp/e/program/lunarpolar/.

[6] Lee, D. E., *White Paper: Gateway Destination Orbit Model: A Continuous 15 Year NRHO Reference Trajectory*, 2019. URL https://ntrs.nasa.gov/citations/20190030294.

[7] Batcha, A. L., Williams, J., Dawn, T. F., Gutkowski, J. P., Widner, M. V., Smallwood, S. L., Killeen, B. J., Williams, E. C., and Harpold, R. E., "Artemis I Trajectory Design and Optimization," *2020 AAS/AIAA Astrodynamics Specialist Conference*, 2020.

[8] McCarthy, B., "Cislunar trajectory design methodologies incorporating quasi-periodic structures with applications," Ph.D. dissertation, Purdue University, 2022.

[9] Lo, M. W., Williams, B. G., Bollman, W. E., Han, D., Hahn, Y., Bell, J. L., Hirst, E. A., Corwin, R. A., Hong, P. E., Howell, K. C., et al., "Genesis mission design," *The Journal of the astronautical sciences*, Vol. 49, 2001, pp. 169–184.

[10] Folta, D. C., Woodard, M., Howell, K., Patterson, C., and Schlei, W., "Applications of multi-body dynamical environments: the ARTEMIS transfer trajectory design," *Acta Astronautica*, Vol. 73, 2012, pp. 237–249.

[11] Gomez, G., Jorba, A., Masdemont, A., and Simo, C., "Study of the transfer between halo orbits," *Acta Astronautica*, Vol. 43, No. 9-10, 1998, pp. 493–520.

[12] Grebow, D., "Generating periodic orbits in the circular restricted three-body problem with applications to lunar south pole coverage," M.S. thesis, Purdue University, 2006.

[13] Steves, B. A., Maciejewski, A. J., and Hendry, M., *Chaotic Worlds: From Order to Disorder in Gravitational N-Body Dynamical Systems*, Vol. 227, Springer Science & Business Media, 2006.

[14] Howell, K. C., and Keeter, T. M., "Station-keeping strategies for libration point orbits- Target point and Floquet Mode approaches," *Spaceflight mechanics 1995*, 1995, pp. 1377–1396.

[15] Williams, D., and Howell, K., "A Comparison of Station-Keeping Strategies for Halo Orbits," *AAS/AIAA Astrodynamics Specialist Conference*, 2023.

[16] Marchand, B. G., "Spacecraft formation keeping near the libration points of the Sun-Earth/Moon system," Ph.D. dissertation, Purdue University, 2004.

[17] Henry, D. B., and Scheeres, D. J., "Quasi-Periodic Orbit Transfer Design via Whisker Intersection Sets," *Journal of Guidance, Control, and Dynamics*, 2023, pp. 1–16.

[18] Bonasera, S., "Incorporating Machine Learning into Trajectory Design Strategies in Multi-Body Systems," Ph.D. dissertation, University of Colorado at Boulder, 2022.

[19] Gómez, G., and Mondelo, J. M., "The dynamics around the collinear equilibrium points of the RTBP," *Physica D: Nonlinear Phenomena*, Vol. 157, No. 4, 2001, pp. 283–321.

[20] Olikara, Z. P., and Scheeres, D. J., "Numerical method for computing quasi-periodic orbits and their stability in the restricted three-body problem," *Advances in the Astronautical Sciences*, Vol. 145, No. 911-930, 2012, pp. 911–930.

[21] Jain, D., "Transfer trajectory design strategies informed by quasi-periodic orbits," M.S. thesis, Purdue University, 2023.

[22] Jorba, À., "Numerical computation of the normal behaviour of invariant curves of n-dimensional maps," *Nonlinearity*, Vol. 14, No. 5, 2001, p. 943.

[23] Baresi, N., and Scheeres, D. J., "Quasi-periodic invariant tori of time-periodic dynamical systems: Applications to small body exploration," *Proceedings of the International Astronautical Congress*, International Astronautical Federation Paris, France, 2016, pp. 9–26.

[24] Gomez, R., "Exploring The Trade Space for Two-Maneuver Transfers from Earth to Cislunar Libration Point Orbits," M.s. thesis, Purdue University, 2021.

[25] McCarty, S. L., Burke, L. M., and McGuire, M., "Parallel monotonic basin hopping for low thrust trajectory optimization," *2018 Space Flight Mechanics Meeting*, 2018, p. 1452.

[26] Lantoine, G., "Efficient NRHO to DRO transfers in cislunar space," 2017.

[27] Vutukuri, S., "Spacecraft trajectory design techniques using resonant orbits," M.S. thesis, Purdue University, 2018.

[28] Pritchett, R. E., "Strategies for low-thrust transfer design based on direct collocation techniques," Ph.D. dissertation, Purdue University, 2020.

[29] Pino, B. J. P., "Energy-informed strategies for low-thrust trajectory design in cislunar space," Ph.D. dissertation, Purdue University, 2020.

[30] Zimovan-Spreen, E. M., Howell, K. C., and Davis, D. C., "Dynamical Structures Nearby NRHOs with Applications to Transfer Design in Cislunar Space," *The Journal of the Astronautical Sciences*, Vol. 69, No. 3, 2022, pp. 718–744.

[31] Muralidharan, V., and Howell, K. C., "Stretching directions in cislunar space: Applications for departures and transfer design," *Astrodynamics*, Vol. 7, No. 2, 2023, pp. 153–178.

[32] McCarthy, B., and Howell, K., "Construction of Heteroclinic Connections Between Quasi-Periodic Orbits in the Three-Body Problem," *The Journal of the Astronautical Sciences*, Vol. 70, No. 4, 2023, pp. 1–16.

[33] Wächter, A., and Biegler, L. T., "On the implementation of an interior-point filter line-search algorithm for large-scale nonlinear programming," *Mathematical Programming*, Vol. 106, No. 1, 2005, p. 25–57. https://doi.org/10.1007/s10107-004-0559-y.

[34] LaFarge, N. B., "Reinforcement Learning Approaches for Autonomous Guidance and Control in a Low-Thrust, Multi-Body Dynamical Environment," Ph.D. dissertation, Purdue University Graduate School, 2023.

[35] Bell, J. L., "Primer vector theory in the design of optimal transfers involving Libration Point orbits," Ph.D. dissertation, Purdue University, School of Aeronautics and Astronautics, 1995.